Mass Determination Methods At Large Hadron Collider

A THESIS

submitted for the Award of Ph.D. degree of

MOHANLAL SUKHADIA UNIVERSITY

in the

Faculty of Science

by

Abhaya Kumar Swain

Under the Supervision of

Dr. Partha Konar

Associate Professor

Theoretical Physics Division

Physical Research Laboratory

Ahmedabad, India.

DEPARTMENT OF PHYSICS
MOHANLAL SUKHADIA UNIVERSITY
UDAIPUR
Year of submission: 2016

To

My Parents and Teachers

DECLARATION

I, **Mr. Abhaya Kumar Swain***, S/o Mr. Alekha Swain, resident of Room No. J115, PRL Navarangapura Hostel, Navarangapura, Ahmedabad, Gujarat 380009, hereby declare that the research work incorporated in the present thesis entitled,* **"Mass Determination Methods At Large Hadron Collider"** *is my own work and is original. This work (in part or in full) has not been submitted to any University for the award of a Degree or a Diploma. I have properly acknowledged the material collected from secondary sources wherever required. I solely own the responsibility for the originality of the entire content.*

Date:

(Abhaya Kumar Swain)

CERTIFICATE

I feel great pleasure in certifying that the thesis entitled, **"Mass Determination Methods At Large Hadron Collider"** embodies a record of the results of investigations carried out by Mr. Abhaya Kumar Swain under my guidance. He has completed the following requirements as per Ph.D regulations of the University.

(a) Course work as per the university rules.

(b) Residential requirements of the university.

(c) Regularly submitted six monthly progress reports.

(d) Presented his work in the departmental committee.

(e) Published minimum of one research papers in a refereed research journal.

I am satisfied with the analysis, interpretation of results and conclusions drawn. I recommend the submission of thesis.

Date:

Dr. Partha Konar
(Thesis Supervisor)
Associate Professor, THEPH,
Physical Research Laboratory,
Ahmedabad - 380 009

Countersigned by

Head of the Department

Acknowledgements

With the end of my thesis, a dream come true project and depicts half a decade research experience of mine, would not have been possible without the succor of many people. I take this opportunity to thank them for being so helpful and offered me nothing short of amazing experience.

First of all, I would like to offer my profoundest gratitude to my PhD supervisor Dr. Partha Konar, for his invaluable guidance, support and encouragement to pursue research in the field of High Energy Physics. I am privileged to have a mentor like him in my research career. He is really a cool guy, puts zero restrictions in any manner, including lifestyle and research style. Specifically I like the part when he would encourage me and my fellow friend to go for some exotic trip outside Ahmedabad. He also motivates to go for jogging every day which again I like very much. Finally, he is an amazing person and a great cook and I thank him for those delicious dinners in his home.

I take the pleasure of thanking the doctoral scientific committee (DSC) for their continuous evaluation of my research work and feedback which helped me revamp my research work. The DSC members include my supervisor and two experts, Prof. Saurabh D. Rindani and Prof. Subhendra Mohanty. I also thank them for checking my thesis with remarkable forbearing and recommending valuable corrections. I am grateful to Prof. Srubabati Goswami, Prof. Raghavan Rangarajan, Dr. Bijaya K. Sahoo, Dr. Navinder Singh, Dr. Namit Mahajan who taught me in the PhD course work. I am also thankful to Prof. H. Mishra, Dr. J. R. Bhatt, Prof. A. S. Joshipura, Prof. U. Sarkar and other faculty members of PRL who encouraged and inspired me in various way during this period.

My office-mates in PRL are really amazing fellows. Thank you Tanmoy, Gulab bhai, Ujjal da, Monojit, Lata didi, so much for helping me in many instances of my research life starting from technical research difficulties to complex physics concepts. Apart from research, they also contributed coherently in many other aspects which resulted in many positive outcomes. I also thank Gulab bhai, Ujjal *da and Tanmoy for proofreading my thesis with great patience and suggest many valuable corrections.*

More importantly, the PhD period in PRL would not have been this smooth as it were without my friends. They fortified me from tension and stress, holding the paramount importance in my healthy and ebullient lifestyle during this period. I express my sincere thanks to you Ikshu, Manu, Tanmoy, Shraddha, Anirban, Kuldeep, Guru, Arun, Girish, Chithrabhanu, Gaurav, Sanjay, Alok for helping me selflessly.

Special thanks to Ikshu, Manu, Tanmoy, Shraddha and Anirban for your kind and supporting nature from which I benefited in various occasions.

I am grateful to my seniors: Shrema, Avdhesh, Ranjita, Sasmita, Gaurav, Girish, Arko, Damodararao, Bhavya, Abhishek, Sudip, Diganta, Ila, Mansi, Nabyendu, Dillip, Yashpal, Gaveshna, Tanushree, Joydeep, Suman, Souvik, whose advice and guidance were very much helpful. I am also thankful to my juniors: Newton, Pankaj, Venkatesh, Rupa, Chandana, Bivin, Rukmini, Chandan, Bhavesh, Aman, Vishnudath, Bharti, Pradeep, Soumik, Niharika, Kiran, Anil, Akanksha, Kaustav, Naman, Harsh, Gulshan, Nidhi, Shefali, Richa, Arvind, Ashish, Balbeer, who cheered me throughout my stay in PRL.

I am extremely thankful to the Physical Research Laboratory (PRL), Ahmedabad, India for giving me a chance to learn, discuss and contribute in the frontiers of High Energy Physics which is a vibrant as well as really vast research field. I am also immensely benefited from PRL services, computer center and its computational facilities, library, transport etc. without their support carrying out research work would have been very difficult.

Finally, I express my wholehearted gratitude towards my parents without their perpetual support I would not have achieved this. I also sincerely thanks my sisters for their love and encouragement in making this possible.

Abhaya

ABSTRACT

The remarkable discovery of the Higgs boson at the Large Hadron Collider filled the last missing bit of the Standard Model and marked the beginning of a new era of searching for physics beyond the SM. TeV scale new physics, if it exists, should show up at the Large Hadron Collider. Among all new physics models, dark matter motivated theories are of particular interest. The dark matter signals in the Large Hadron Collider are challenging in respect of discovering them as well as determination of properties like mass, spin *etc.* associated with the new particles in the discovery signal. Study of mass sensitive observables in this regard can not only provide mass and spin information but can also be used as a discovery tool.

In this thesis, we demonstrate how the already available constraint(s) can further sharpen the mass bound variables considering both inclusive and exclusive observables. We have studied the mass bound variables $\sqrt{\hat{S}_{min}}$ and its variants by minimizing the parton level center of mass energy that is consistent with all inclusive measurements. They were proposed to have the ability to measure mass scale of new physics in a fully model independent way. Here we relax the criteria by assuming the availability of partial information of new physics events and thus constrain this mass variable even further. Starting with two different classes of production topology, *i.e.,* antler and non-antler, we demonstrate the usefulness of these variables to constrain the unknown masses. This discussion is illustrated with different examples, from the standard model Higgs production and beyond standard model resonance productions leading to semi-invisible production. We also utilize these constraints to reconstruct semi-invisible events and thus improving the measurements to reveal the properties of new physics.

We further moved to mass-constraining variable M_2, a $(1+3)$-dimensional natural successor of the extremely popular M_{T2}. M_2 possesses an array of rich features having the ability to use on-shell mass constraints in semi-invisible production at a hadron collider. We investigate the consequence of applying a heavy resonance mass-shell constraint in the context of a semi-invisible antler decay topology produced at the LHC. Our proposed variable, under additional constraint, develops a new kink solution at the true masses. This enables one to determine the invisible particle mass simultaneously with the parent particle mass from these events. We analyze a way to measure this kink optimally, exploring the origin and the properties of such interesting characteristics. We also study the event reconstruction capability inferred from this new variable and find that the resulting momenta are unique and well correlated with the true invisible particle momenta. This proposal of reconstruction is demonstrated with a potentially interesting scenario, when the Higgs boson decays into a pair of τ leptons. The LHC has already started exploring this pair production to investigate the properties of Higgs in the leptonic sector. Dominant signatures through hadronic decay of tau, associated with invisible neutrinos compound the difficulty in the reconstruction of such events. Exploiting the already existing Higgs mass bound, this new method provides a unique event reconstruction, together with a significant enhancement in terms of efficiency over the existing methods.

Keywords : Beyond Standard Model, Standard Model, Hadronic Colliders, Particle and resonance production, Higgs, Tau lepton, Event reconstruction.

LIST OF PUBLICATIONS

Publications contributing to this thesis :

1. **Abhaya Kumar Swain** and Partha Konar, "Constrained $\sqrt{\hat{S}_{min}}$ and reconstructing with semi-invisible production at hadron colliders"
arXiv:1412.6624 [hep-ph], **JHEP 1503, 142 (2015)**.

2. **Abhaya Kumar Swain** and Partha Konar, "Mass determination and event reconstruction at Large Hadron Collider"
arXiv:1507.01792 [hep-ph], **Springer Proc.Phys. 174 (2016) 599**.

3. Partha Konar and **Abhaya Kumar Swain**, "Mass reconstruction with M_2 under constraint in semi-invisible production at a hadron collider"
arXiv:1509.00298[hep-ph], **Phys. Rev. D 93, 015021 (2016)**.

4. Partha Konar and **Abhaya Kumar Swain**, "Reconstructing semi-invisible events in resonant tau pair production from Higgs "
arXiv:1602.00552[hep-ph], **Phys.Lett.B757, 211 (2016)**.

Other publications :

1. Partha Konar, Pankaj Sharma and **Abhaya Kumar Swain**, "Exploring CP violating phase in τ-lepton Yukawa coupling from $H \to \tau^+\tau^-$ decays at the LHC",
Manuscript under preparation.

List of Abbreviations

SM	Standard Model
BSM	Beyond Standard Model
SUSY	Supersymmetry
MSSM	Minimal Supersymmetric Standard Model
RH	Right-Handed
LH	Left-Handed
VEV	Vacuum Expectation Value
EW	Electroweak
EWSB	Electroweak Symmetry Breaking
SSB	Spontaneous Symmetry Breaking
LHC	Large Hadron Collider
DM	Dark Matter
HS	Hard Scattering
UTM	Upstream Transverse Momentum
ISR	Initial State Radiation
FSR	Final State Radiation
MAOS	M_{T2} assisted on-shell

Contents

List of Tables

List of Figures

Chapter 1

Introduction

"We keep moving forward, opening new doors, and doing new things, because we are curious and curiosity keeps leading us down new paths."
–Walt Disney

We, the Humans, are curious about the origin/formation and the evolution of our Universe from the beginning of human life on the Earth. Our curiosity drives us to form a theory to explain the observed phenomena in nature and test the theory by designing suitable experiments. Now, at this point of time, with the advancement of many experiments, the most successful theory that explains the microscopic nature of our Universe is the Standard Model (SM) of particle physics. The SM [1, 2] is the description that tries to include all the fundamental building blocks of matter in our Universe and the interactions between them. It is a gauge theory based on some symmetry principles. Once these symmetries are respected, all fundamental fermions and bosons need to be massless, which is contradictory to observations. Spontaneous symmetry breaking (SSB) is the mechanism which gives masses to these fundamental particles without explicitly breaking the symmetry of the theory. In this chapter, we discuss briefly the structure of the SM and the SSB mechanism and the motivation for the physics beyond the Standard Model (BSM). We also discuss the ongoing Large Hadron

Collider (LHC) and generic production mechanisms of new particles. If new exotic particle production is observed at the LHC, measurement of their masses and momenta remains a challenge, if some of their final decay products are invisible. This being the basic theme of this thesis, we further discuss challenges involved pointing out some of the techniques. Finally, we present an overview of remaining chapters of the thesis.

1.1 The Standard Model of particle Physics

Fundamental particles are basic building blocks of everything we see around us. All matter in the Universe consists of two types of fundamental particles – quarks and leptons, which are spin-1/2 fermions. Each type comes in three generations. The first generation particles are the lightest and stable, the second and third generation particles are heavier and unstable which eventually decay into lighter ones[1]. Hence, all matter we see around us now is mostly made up of first generation particles. The first generation quarks are named as up and down, charm and strange are quarks of the second generation followed by the third generation top and bottom quarks. The quarks have color charge and fractional electric charge associated with them. But color confinement ensures that they combine in such a way as to result in colorless mesons and baryons. Similarly, the electron and electron-neutrino are first generation leptons, the second and third generation leptons are muon, muon-neutrino and tau, tau-neutrino, respectively. Neutrinos are electrically neutral and massless in the Standard Model. The remaining three leptons (electron, muon and tau) are electrically charged with the electron being the lightest and stable, while tau is the heaviest and unstable.

There exist four fundamental interactions in Nature. They are strong, electromagnetic, weak and gravitational interactions. These forces are responsible for the interaction of fundamental particles among themselves. These first three interactions are mediated via a spin-1 boson. The electromagnetic and strong interaction are mediated via the photon and gluons which are massless, while the

[1] Note that neutrinos in the SM are stable particles and they do not decay, irrespective of which generation they belong to.

weak force is mediated by massive W and Z bosons. Gravitational interaction or its mediator graviton is not included in the SM. Among the four fundamental forces the gravitational force is the weakest and it has infinite range. The electromagnetic interaction is also of infinite range but much stronger than the gravitational force. The strong interaction is the strongest force among all and the weak force is the second weakest interaction. In addition, both the strong and weak forces are short-ranged and act at the sub-atomic level.

The Standard Model is the description of the interactions which include all the fundamental particles and three of the four forces listed above. The SM does not include gravitational interaction. In addition, it is a unified description in terms of a gauge theory (one that is invariant under a set of local transformations where the parameters are functions of space and time) of all fundamental particles. The underlying gauge group of the SM is $SU(3)_c \otimes SU(2)_L \otimes U(1)_Y$, where c, L and Y stand for color, left-handed isospin and hyper charge, respectively. The SM has been extremely successful in explaining a wide range of experimental observations. The recent discovery of the last remaining piece of the SM, the Higgs boson, by the ATLAS [3] and the CMS [4] collaborations at the LHC makes this model even more appealing. The Higgs boson is the particle which is responsible for generating mass terms in the theory for all the fermions and weak gauge bosons without explicitly breaking the SM symmetry. The field content of the SM and the corresponding quantum numbers are listed in table 1.1.

The Lagrangian of the SM with the above symmetry and particle contents is

$$\mathcal{L}_{SM} = \mathcal{L}_{\text{Gauge}} + \mathcal{L}_{\text{Fermion}} + \mathcal{L}_{\text{Higgs}}, \tag{1.1}$$

the three contributions on the right-hand side being as described below.

Gauge and fermion sector

The gauge boson of the abelian group $U(1)_Y$ in the SM gauge structure above

Fields (particles)	(Color(c), Isospin(T_3), Hypercharge(Y)) $SU(3)_c \otimes SU(2)_L \otimes U(1)_Y$	Electric charge(Q) $Q = T_3 + Y/2$
$q_L = \begin{pmatrix} u_L \\ d_L \end{pmatrix}$	$\begin{pmatrix} (3, +1/2, +1/3) \\ (3, -1/2, +1/3) \end{pmatrix}$	$\begin{pmatrix} +2/3 \\ -1/3 \end{pmatrix}$
u_R	(3, 0, +4/3)	+2/3
d_R	(3, 0, −2/3)	−1/3
$\ell_L = \begin{pmatrix} \nu_L \\ e_L \end{pmatrix}$	$\begin{pmatrix} (1, +1/2, -1) \\ (1, -1/2, -1) \end{pmatrix}$	$\begin{pmatrix} 0 \\ -1 \end{pmatrix}$
e_R	(1, 0, −2)	−1
$H = \begin{pmatrix} \phi^+ \\ \phi^0 \end{pmatrix}$	$\begin{pmatrix} (1, +1/2, +1) \\ (1, -1/2, +1) \end{pmatrix}$	$\begin{pmatrix} +1 \\ 0 \end{pmatrix}$

Table 1.1: The SM field content and the quantum numbers are listed with charges c, T_3 and Y for color, isospin and hypercharge of a particle, respectively.

is denoted by B^μ. The $SU(2)_L$ has three generators and the gauge bosons lie in the adjoint representation of the group. Gauge bosons in this group are represented by W^α_μ ($\alpha = 1, 2, 3$). These gauge bosons (both W^α_μ and B_μ) are not physical but their linear combinations (photon, $W^\pm$ and Z bosons) are, and they mediate electroweak interactions. Lastly, the $SU(3)_c$ describes strong interactions with eight generators and there are eight gauge bosons, viz., the gluons. The theory of strong interactions which is based on the gauge group $SU(3)_c$ is known as quantum chromodynamics (QCD)[5, 6]. All these bosons are described by spin-1 vector fields. The Lagrangian for this part is given by,

$$\mathcal{L}_{\text{Gauge}} = -\frac{1}{4} B_{\mu\nu} B^{\mu\nu} - \frac{1}{4} W^\alpha_{\mu\nu} W^{\alpha\ \mu\nu} - \frac{1}{4} F^i_{\mu\nu} F^{i\ \mu\nu}, \tag{1.2}$$

with

$$B_{\mu\nu} = \partial_\mu B_\nu - \partial_\nu B_\mu, \tag{1.3}$$

$$W^\alpha_{\mu\nu} = \partial_\mu W^\alpha_\nu - \partial_\nu W^\alpha_\mu - g\epsilon^{\alpha\beta\gamma} W^\beta_\mu W^\gamma_\nu, \tag{1.4}$$

$$F^i_{\mu\nu} = \partial_\mu F^i_\nu - \partial_\nu F^i_\mu - g_s f^{ijk} F^j_\mu F^k_\nu, \tag{1.5}$$

where F^i_μ represent gluons (with $i = 1, 2, \ldots, 8$). g and g_s are coupling constants of $SU(2)_L$ and $SU(3)_c$ gauge groups , respectively. The $\epsilon^{\alpha\beta\gamma}$ and f^{ijk} are the structure constants of the corresponding Lie algebras.

Fermions in the SM can be categorized based on their representations under $SU(2)_L$ as can be seen in table 1.1. Left-handed leptons form a $SU(2)_L$ doublet, while the right-handed leptons are singlets. Similarly, the left-handed quarks are $SU(2)_L$ doublets while the right-handed quarks transforms as singlets. The Lagrangian for the fermion kinetic term is

$$\mathcal{L}_{\text{Fermion}} = \sum i\bar{\psi}\not{D}\psi, \tag{1.6}$$

with $\not{D} = \gamma^\mu D_\mu$, where D_μ is the corresponding covariant derivative defined as,

$$D_\mu = \partial_\mu + ig_s\frac{\lambda.F_\mu}{2} + ig\frac{\sigma.W_\mu}{2} + ig^{'}YB_\mu, \tag{1.7}$$

where $g^{'}$ is the $U(1)_Y$ gauge coupling. The generators of $SU(3)_c$, λ^i (with $i = 1, 2, \ldots, 8$) , are the Gell-Mann matrices. Similarly, the generators of $SU(2)_Y$, σ^i, (with $i = 1, 2, 3$), are the Pauli matrices.

Higgs mechanism

One can notice that an explicit mass term for fermions will violate the gauge invariance. This is because the mass term mixes the left and right-handed fermions which are coming from different multiplets of the $SU(2)_L$. Similarly, an explicit gauge boson mass term also breaks gauge invariance. But from experimental observations, we know that some of the gauge bosons as well as all the fermions[2] are massive. The existence of massive fundamental particles and massive gauge bosons can be understood from spontaneous breaking of the SM symmetry, known as the Higgs mechanism [7–10]. In this mechanism the theory (*i.e.*, Lagrangian) remains invariant under the SM symmetry but the ground state (*i.e.*, vacuum) does not. To achieve this, one needs to introduce a complex

[2] Although in the SM the neutrinos are massless, the neutrino oscillation experiments show that they have tiny non-zero mass.

scalar field ϕ which is a doublet under the $SU(2)_L$ gauge group as given by,

$$\phi = \begin{bmatrix} \phi^+ \\ \phi^0 \end{bmatrix}. \tag{1.8}$$

The gauge invariant Lagrangian corresponding to this scalar field is

$$\mathcal{L}_{Higgs} = (D_\mu\phi)^\dagger(D_\mu\phi) - V(\phi), \tag{1.9}$$

with

$$V(\phi) = -\mu^2(\phi^\dagger\phi) + \lambda(\phi^\dagger\phi)^2, \tag{1.10}$$

$$D_\mu = \partial_\mu + ig\frac{\sigma.W_\mu}{2} + ig^{'}YB_\mu, \tag{1.11}$$

where $V(\phi)$ and D_μ are the scalar potential and the covariant derivative associated with the scalar field, respectively. The parameters μ^2 and λ are positive. The potential $V(\phi)$ has a minimum at

$$\phi^\dagger\phi = \frac{\mu^2}{2\lambda}. \tag{1.12}$$

The real part of the neutral component of the scalar doublet gets a vacuum expectation value (vev) and we can write this as

$$\langle\phi_0\rangle = \frac{1}{\sqrt{2}}\begin{bmatrix} 0 \\ v \end{bmatrix} \tag{1.13}$$

with $v = \frac{\mu}{\sqrt{\lambda}}$. The perturbative calculation would require expansions around this minimum as

$$\phi = \frac{1}{\sqrt{2}}\begin{bmatrix} 0 \\ v + h(x) \end{bmatrix} \tag{1.14}$$

where $h(x)$ is the quantum fluctuation around this minimum. Using eqs. 1.14 and 1.10 we get a mass term for the Higgs field h as $m_h = \sqrt{2\lambda v^2}$. Similarly, using eq. 1.14 and the first term of eq. 1.9 we get the mass terms for the gauge bosons as

$$|D_\mu\phi|^2 = \frac{1}{2}(\partial_\mu h)^2 + \frac{g^2v^2}{4}W^+W^- + \frac{v^2}{8}(gW_\mu^3 - g^{'}B_\mu)^2 + \ldots \quad (1.15)$$

$$= \frac{1}{2}(\partial_\mu h)^2 + \frac{g^2v^2}{4}W^+W^- + \frac{g^2v^2}{8\cos^2\theta_W}Z_\mu Z^\mu + \ldots, \quad (1.16)$$

where the ellipses in previous equations contains the interaction terms and $W^\pm$, Z^μ and A^μ are the charge eigenstates of the gauge bosons defined as,

$$W_\mu^\pm = \frac{1}{\sqrt{2}}(W_\mu^1 \pm iW_\mu^2), \quad (1.17)$$

$$Z_\mu = \cos\theta_W W_\mu^3 - \sin\theta_W B_\mu, \quad (1.18)$$

$$A_\mu = \cos\theta_W B_\mu + \sin\theta_W W_\mu^3. \quad (1.19)$$

Here θ_W is the Weinberg angle which is defined as

$$\tan\theta_W = \frac{g^{'}}{g}. \quad (1.20)$$

Now the mass of the gauge bosons are

$$m_W = \frac{1}{2}gv, \quad (1.21)$$

$$m_Z = \frac{1}{2}v\sqrt{g^2 + g'^2}, \quad (1.22)$$

$$m_A = 0. \quad (1.23)$$

Thus, the gauge bosons W and Z acquire masses and the photon remains massless which results from the spontaneous breaking of the SM gauge group. The symmetry group $U(1)_Q$ remains an unbroken symmetry of nature which leads to a massless photon.

The fundamental fermions, except neutrinos, also get their masses through the Higgs mechanism. The Lagrangian corresponding to the interaction of the first generation fermions with the scalar is,

$$\mathcal{L}_{Yukawa} = -Y_u\bar{q_L}\tilde{\phi}u_R - Y_d\bar{q_L}\phi d_R - Y_e\bar{\ell}_L\phi e_R + h.c., \quad (1.24)$$

where $\tilde{\phi} = i\sigma_2\phi^*$ and Y_i $(i = u, d, e)$ is the Yukawa coupling for the fermions of the first generation. Similar terms can be written for the other two generations. The mass of the fermions after spontaneous symmetry breaking, using eq. 1.14 in eq. 1.24, is $m_f = \frac{Y_i v}{\sqrt{2}}$.

1.2 Need for physics beyond the Standard Model

Besides the fact that the SM attains humongous success both theoretically and experimentally, it has a number of drawbacks. There is a series of experimental observations which are not explained by the SM, although they do not negate it either. We have inferred the presence of dark matter (DM), from several astrophysical observations which tell us that the DM makes up roughly 80% of the total matter content of our Universe. The DM particle, if it is some exotic fundamental one, needs to be colorless, electrically neutral and interacts weakly with the SM particles. It manifests its presence through the gravitational interaction. The SM does not include a particle which can qualify as a good DM candidate. Hence, DM should be a particle coming from some as yet unknown physics beyond the SM. Also, our Universe is found to be populated with baryonic matter which implies matter-antimatter asymmetry. This asymmetry can not be explained by the SM and requires BSM. The observation of neutrino oscillation implies the existence of tiny but non-zero neutrino mass. This cannot be described by the SM because the SM does not include any right-handed neutrino. To explain neutrino mass one needs to invoke BSM.

In addition, there are a number of open questions of rather fundamental nature to believe that there must be physics beyond the SM, where the SM is one great low energy description of effective theory. In the SM there is no a priori reason for existence of three generation of fermions and their mass range is really vast. The gravitational interaction is outside the SM description. More importantly, the observed Higgs mass (125 Gev) receives a large quantum correction and must cancel up to 34 decimal places in order to obtain a finite quantity, which is unnatural. This arises because of the difference between the involved energy scales: the electroweak scale and the Planck scale. This is known as the hierarchy problem. Numerous models beyond the Standard Model were constructed to accommodate some of these phenomena with the general belief that the scale of new physics is just around the corner in the multi-TeV range. Unfortunately, the Large Hadron Collider has not observed any indication of new physics so far. If any of these TeV-scale BSM theories exist in nature, then it should manifest its signature at the next LHC run. A scenario with a positive signal essentially necessitates the determination of masses, spins, and couplings etc. of the new particles associated with the new physics.

1.3 Large Hadron Collider

In this section we briefly discuss the LHC. The LHC is the largest particle accelerator ever built in human history, installed at the European particle physics laboratory CERN, situated across the border between Switzerland and France. It consists of a circular tunnel of 27 km circumference which is approximately 100 meters below the ground in which two beam pipes are present. Inside each beam pipe proton beams are accelerated, in opposite direction, with the highest possible speed using superconducting magnets and other accelerator components. The speed and direction of the proton beams are controlled by the electric and magnetic fields. In its run-I, the LHC had gathered 5 fb^{-1} and 25 fb^{-1} of data with 7 TeV and 8 TeV center of mass (CM) energy of collision, respectively. After that it had undergone a long shut down and upgraded its CM energy of collision to 13 TeV and now it has already gathered around 5 fb^{-1} data in its run-II in 2016.

The detectors are the most important part of the LHC and is placed at the crossing points of the two proton beams as shown in fig. 1.1. There are four crossing points where detectors ATLAS[12], CMS[13], ALICE[14], LHCb[15] are installed among which the first two are general purpose detectors and the last two are dedicated for heavy ion collisions and B hadron studies, respectively. The CMS detector consists of several layers of detector material that use differ-

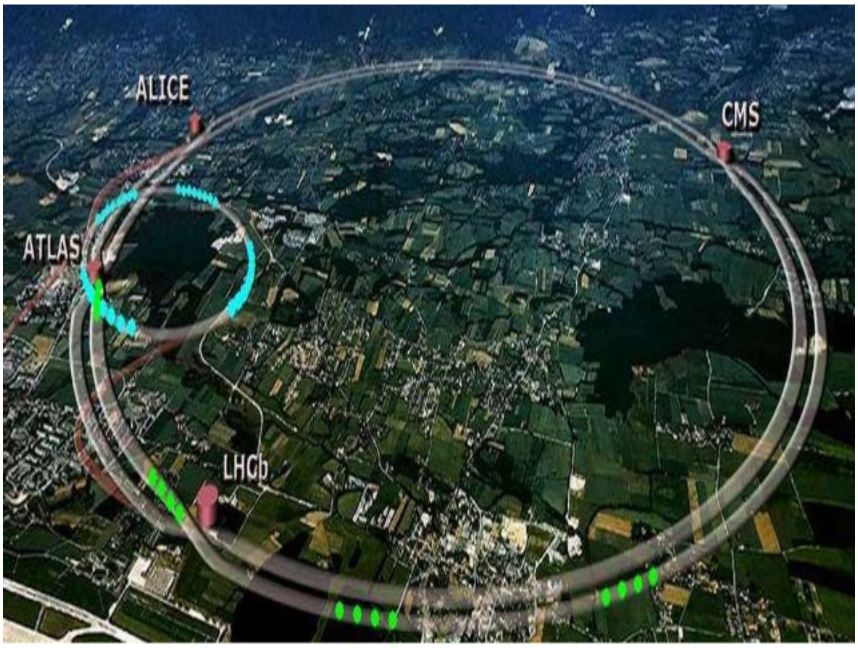

Figure 1.1: Representation of the LHC position with its two beam pipes. It also captures the positions of different detectors ATLAS, CMS, ALICE and LHCb. ATLAS and CMS are the general purpose detectors while ALICE and LHCb are specialized for heavy ion collision and bottom quark studies (taken from [11]).

ent properties of particles and measure their energy and momenta. The different components of the CMS detector are silicon tracker, electromagnetic calorimeter, hadron calorimeter and lastly the muon chamber. The length of the detector is 22 meters with diameter 15 meters and the approximate weight is 14×10^6 kilograms. To measure the properties of charged particles, there is a superconducting solenoid which in its running condition can produce a magnetic field of 3.8 Tesla. A pictorial representation of CMS detector is shown in fig. 1.2.

The particles produced from the collision of two proton beams first encounter the silicon tracker. It is made up of silicon pixels and silicon strip detector, which measures the trajectory of the charged particle as it traverses through it. Due to the presence of a strong magnetic field, the trajectories of the charged particles will be curved because of the Lorentz force acting on it. From the nature of the tracks the momentum of the charged particles can be measured. After the tracker, the next detector component is the electromagnetic calorimeter where electron, photon etc. deposit their energy. The third major part is the hadron calorimeter in which hadron like proton, neutron, pion etc. deposit energy. Fi-

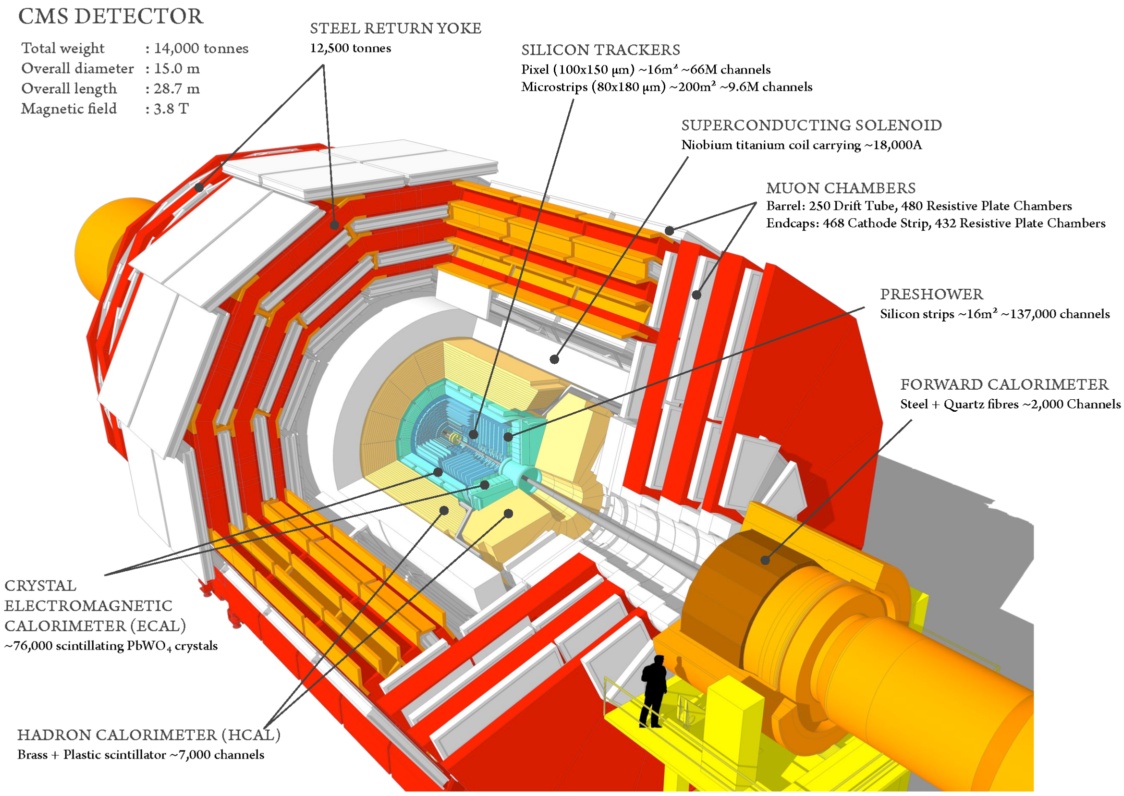

Figure 1.2: A schematic representation of the multipurpose CMS detector (adapted from ref. [16]).

nally, the last part of the detector is the muon chamber which is used to stop the muon and measure its energy. As neutrinos are weakly interacting particles, they escape the detector without detection. The signatures displayed by different particles are represented in fig. 1.3.

We have mentioned in the last paragraph that the momentum of a charged particle can be determined by measuring the radius of curvature of the trajectory exhibited by it in the tracker. The radius of curvature in terms of the momentum is

$$\frac{1}{r} = \frac{qB}{p}, \tag{1.25}$$

where q is the electric charge of the particle, B is the applied magnetic field and p is the momentum of the particle. Hence, the momentum can be measured with the assumption of unit electric charge. The energy loss of a heavy charged particle inside a detector, using the Bethe-Block formula, is proportional to the

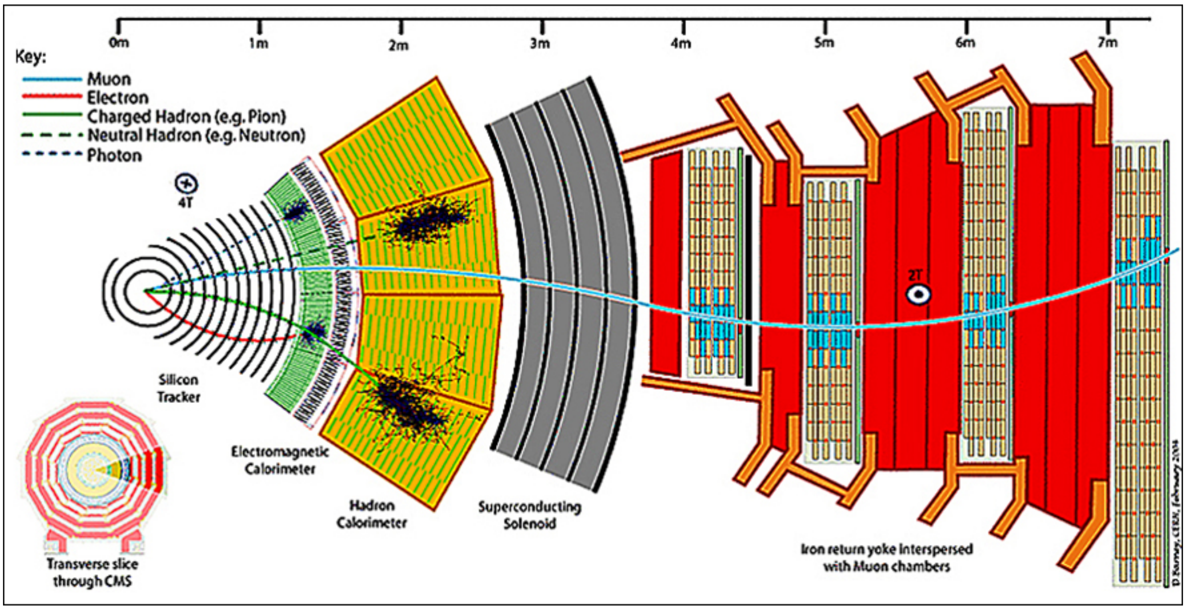

Figure 1.3: A pictorial description of a transverse slice of the CMS detector is shown. The characteristic signature of stable particles are shown as different colored/dashed lines. The charged particles display tracks in the tracker and deposit energy in the calorimeter while neutral particles deposit energy in the corresponding calorie meter (taken from [17]).

charge q and the speed β of the particle as follows,

$$\frac{dE}{dx} \propto (q/\beta)^2. \tag{1.26}$$

Therefore, by assuming unit electric charge and measuring the energy loss inside the detector, one can calculate the speed of the particle. Now, using eqs. 1.25 and 1.26 the mass of the corresponding particle can be determined. Any measurement in a detector follows a coordinate system. In the CMS conventionally the center of the coordinate system is taken as collision point of the two protons. The radially inward direction of the LHC ring is the $x-$direction, the vertically upward direction is the $y-$axis and the proton beam direction is the $z-$direction. The commonly used coordinate system is the cylindrical coordinate system where the radial distance r is measured from the interaction point, ϕ is the azimuthal angle with $x = r\cos\phi$ and $y = r\sin\phi$. The longitudinal component is taken care of by the pseudorapidity $\eta = -\ln\Big(\tan(\theta/2)\Big)$ where θ is measured from z-axis.

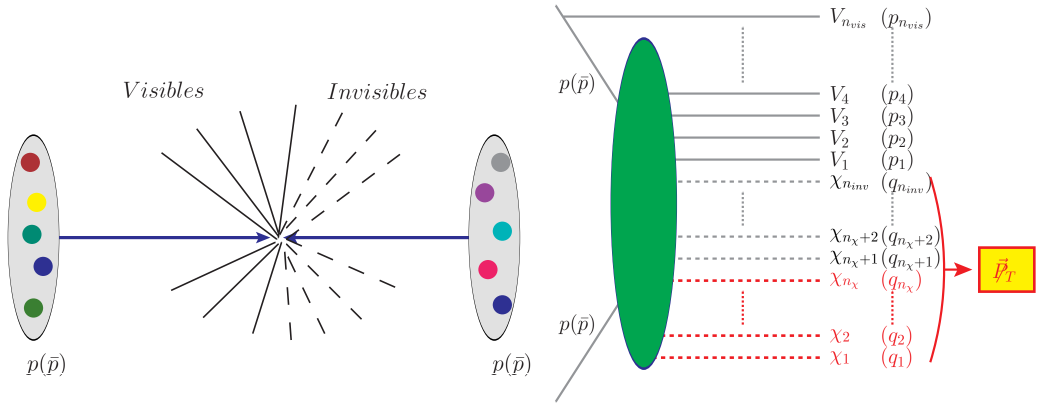

Figure 1.4: A generic picture (left panel) of a proton-proton collision at the LHC; some visible particles along with some invisible particles are produced. A particle is referred as visible if the energy and momentum of it can be determined in the detector and invisible otherwise. The examples of invisible particle are neutrinos and dark matter candidates and visible particles are electron, muon, photon, pion etc. In the reaction each parton (quarks and gluons) takes a fraction of the proton momenta. In the right panel, a generic topology as expected theoretically is shown. The solid black lines represent the SM visible particles which can come from the hard scattering (HS) or initial state radiation (ISR). Dashed lines portray invisible particles with black lines refers to SM neutrinos while red lines are DM particles.

Commonly used coordinates to express the momentum of any particle are the η, ϕ and the transverse momentum associated with it.

1.4 Mass determination methods at LHC

After a brief discussion about the LHC, in this section we talk about various mass determination methods which can be used for measuring the mass of the new particles. Before we talk about mass measurement methods, we would like to briefly mention the generic event topology through which new particles are produced at the LHC. A generic event topology is represented in the right panel of fig. 1.4. Among the final state particles, the black solid lines correspond to SM visible particles V_i, with $i = 1, 2, \ldots, n_{vis}$, where n_{vis} is the number of visible particles, *e.g.*, electron, muon, photon, and jets, whose energy and momentum can be measured in the detector. The SM particles may come from the hard scattering and decay products of some unstable particles (hidden in the green shaded ellipse) or from the initial state radiation (ISR). Dashed lines delineate the invisible particles such as SM neutrinos or DM candidates which remain undetected in the detector. The red dashed lines depict DM particles χ_i, with $i = 1, 2, \ldots, n_\chi$, where n_χ is the number of DM particle produced in the final state. Black dashed lines represent the SM neutrinos χ_i, with $i = n_\chi{+}1, n_\chi{+}2, \ldots, n_{inv}$, where n_{inv} is the total number of invisible particles produced. The identities and masses of the DM particles in this topology may not be same, allowing simultaneous production of different species of DM particles.

For the invisible particle, missing transverse momenta $\vec{\not{P}}_T$ is the only experimentally measured quantity, calculated from the imbalance of transverse momenta produced in such events. This imbalance is evident from the fact that, using momentum conservation, the transverse momentum of the final state particles should add to zero, as it does for the initial partons. The inability to determine the energy and longitudinal component of the invisible particle is partly because of the challenges associated with the hadron collider. The challenges include partial knowledge of the incoming parton momenta, that the boost along the beam direction is unknown, and that the CM energy of collision is also not known.

In the left panel of fig. 1.4, we discuss the production of a similar generic event topology at a hadron collider and describe the challenges associated with it. The momenta of the two colliding protons are denoted by $\{\sqrt{S}/2, 0, 0, \sqrt{S}/2\}$ and $\{\sqrt{S}/2, 0, 0, -\sqrt{S}/2\}$, where S is the CM energy of the collider. In high energy colliders, the collision between protons is effectively a collision between the constituent partons which carry an unknown fraction of corresponding proton momenta. So the parton momenta before collision are written in terms of these two unknown fractions x_1 and x_2. As a result the parton level CM energy of collision, $\hat{s} = x_1 x_2 S$, is unknown. The boost along the beam direction, $\beta = \frac{x_1 - x_2}{x_1 + x_2}$, is also not known.

In such a scenario, if some of the final state particles go undetected from the production of neutrinos or dark matter candidate, the kinematics of such semi-invisible event remains undetermined. Hence, a subset of the degrees of freedom remains unknown. A typical production of presence of dark matter in the event even worsens the scenario. The stability of dark matter, in most of the BSM theories is ensured by some discrete symmetry, such as R-parity in supersymmetry, KK-parity in Universal Extra Dimension models etc. Once this symmetry is respected, all the heavy BSM particles in such model have to be produced in pairs, subsequently decaying into some lighter BSM resonance together with SM particles (which may or may not be detected) in multiple steps of successive decay. Typically, at the end of each decay chain the lightest BSM particle is produced which is the dark matter particle of that model and escapes the detection. Hence, not one, but at least two massive BSM particles remain hidden in these events. The only way to know their presence, as discussed earlier, is the observation of a sizable $\vec{\not{P}}_T$ in the detector.

Several studies have been performed to determine the masses and spins of the particles in the context of semi-invisible production at the hadronic collider, for some recent reviews, see refs. [18–20]. We classify them based on the topology information as follows[3]:

Global and inclusive variables

These variables are independent of the topology information and hence, do not require any information about the production mechanism of the particles in the event and are defined for a generic topology shown in fig. 1.4. This kind of variables are constructed using only visible particle momenta and missing transverse momenta in the event. Several of them were well known and utilized for long as event selection variables *e.g.*, H_T [21], total visible invariant mass M [22], effective mass M_{eff}, total transverse component of invisible momentum $\not{E}_T$, total visible energy E and total transverse energy E_T in the event. The recently introduced $\hat{s}_{min}$ [23] and its variants $\hat{s}^{sub}_{min}$ and $\hat{s}^{reco}_{min}$ [24] are also constructed as global and inclusive variables for measuring mass scale of new physics. Being topology independent variables, they are also applicable to any decay chain irrespective of whether it has symmetric or asymmetric topology and a simple analytical form is also available. Thus, any generic topology can be assimilated without being

[3]Although we have covered some of the mainstream studies, there are plenty of analysis techniques which we have not included here. Here our choices are motivated by the idea of giving an introduction of the approaches we followed and refined in subsequent chapters.

affected by the combinatorial ambiguity.

Exclusive variables

Exclusive variables are defined based on the topology of the production mechanism and decay processes under consideration. Identical signatures consisting of visible and invisible particles present in the final state can originate from very different topologies which are deeply related to the stabilizing symmetry of the DM. The shape of the visible invariant mass can effectively carry information on topology along with the mass spectrum [25] of the decay chain. The underlying DM stabilizing symmetry can also be probed [25–29] using kinematic edge and cusp in the invariant mass distributions and from the shapes of transverse mass variable M_{T2}. Even the assumption of one particular underlying symmetry allows some fixed number of different topologies from which the correct one can be identified comparing suitable kinematic variables [30]. One expects that the ignorance of the correct topology can add difficulties in solving combinatorial ambiguity [31–34] which is one source of complexity in mass determination methods. This ambiguity becomes more prominent for longer decay chain. This ambiguity can originate from two different sources. Firstly, allocation of the final state particles to the correct decay chain, *i.e.,* deciding from which side of the decay chain some particular states are produced. Secondly, the ordering of the assigned particle in a single decay chain. The hemisphere method [35] and P_T v. M method [32] are introduced to reduce this ambiguity in assigning the correct final state particles to the corresponding decay chain. However, the ordering of the particles is left unresolved. The M_{T2} variable together with invariant mass are also shown to reduce the combinatorics significantly [33]. In the literature several classes of exclusive variables are defined assuming that the correct knowledge of the topology is available and anticipating that the combinatorial ambiguity can be controlled. The exclusive mass determination methods can be categorized as follows:

- ◇ *Edge measurement method*: This method is based on the idea of constructing all possible invariant masses out of visible decay products in each decay chain [36–42]. Each invariant mass has an endpoint which is experimentally observable and these endpoints are related to the unknown masses in the decay chain. To evaluate all the unknown masses by inverting the equations in terms of measured endpoints, one needs sufficient number of independent endpoint measurements. So essentially a long decay chain is necessary to have unique measurement of all the unknown masses. However, this criterion inevitably invites combinatorial ambiguity thereby reducing the effectiveness of the method. This method does not use all the available information like missing transverse momentum $\vec{\not{P}}_T$ in the event.

◇ *Polynomial method*: One tries to utilize all the available information in the event of a particular topology and solve for the unknown masses and momenta [43–47] considering on-shell cascade decay. In the literature, typically the production of two heavy invisible particle is considered in the final state, assuming Z_2 type of DM stabilizing symmetry in the theory. All the unknown invisible momentum components are solved for utilizing mass-shell constraints and missing $\vec{\not{P}}_T$ constraints in the event. It can be shown that one needs to consider long decay chains to solve for all unknowns in the event. Combinatorial ambiguity naturally arises here from the requirement of the long decay chain. Moreover, resulting invisible momenta remain ambiguous due to the existence of multiple solutions originating from non-linear mass-shell constraints [47, 48].

◇ *Transverse mass variable*: Rather than considering full event information, transverse projection of momenta is considered during the calculation. Contrary to the previous cases, even a small decay chain can constrain the masses realistically. In the literature, many variants of transverse mass variables have been studied, such as M_{T2} [49–57], M_{T2}^{sub} [58], M_{CT2} [59, 60], 1D orthogonal decomposition of M_{T2} ($M_{T2\perp}$ and $M_{T2\parallel}$) [61], asymmetric M_{T2} [62, 63] and M_{T2}^{approx} [64], M_{CT} [65–67], and variants $M_{CT\perp}$ and $M_{CT\parallel}$ [68] etc. Among these broad classes of transverse mass-bound variables, we briefly discuss some properties of M_{T2} which is studied widely in the literature. This variable is defined as the constrained minimization of maximum of two transverse masses M_T from both sides of the decay chain. The minimization is done over all possible partitions of missing transverse momenta satisfying the $\vec{\not{P}}_T$ constraint. The variable $M_{T2}(\tilde{m}_{inv})$, expressed as a function of the unknown invisible particle mass, can have an experimentally observed upper bound over many events. This provides a useful correlation between the trial invisible mass $\tilde{m}_{inv}$ and measured upper bound M_{T2}^{max}, which represents the corresponding mass of the ancestor particle (commonly called as mother or parent) responsible for producing all the visible and the invisible particles within the (sub)system. This correlation also satisfies the true yet unknown mass parameters fulfilling the crucial equality $M_{T2}^{max}(m_{inv}^{true}) = m_{mother}^{true}$. Interestingly, one can measure the true mass of both mother and daughter simultaneously by identifying a kink arising due to additional conditions like a two step decay chain [53, 54], extra upfront P_T from ISR [55, 56] or in the subsystem context [58]. In the presence of background, extracting these kinematic endpoint is occasionally troublesome with thinly populated events at the endpoint. Available on-shell constraints of intermediate particles can be exploited in the (1+3) dimensional variable M_2 [69, 70] to improve the number of events appearing at the tail of these distributions.

1.5 Thesis Overview

The thesis is organized as follows. In chapter 2, we briefly discuss the global and inclusive variable $\hat{s}_{min}$ and its sisters $\hat{s}_{min}^{sub}$ and $\hat{s}_{min}^{reco}$. We thereafter discuss the effect of partial topology information on these inclusive variables which results in some interesting new observables . We also talk about the full event reconstruction capability of the new variables and compared the result with the existing ones. In chapter 3, we describe the transverse mass variable, M_{T2}, and its properties which enables one to determine all the unknown masses in a short decay chain. We then discuss a new and interesting observable M_{2Cons} and examine its properties. It has been shown to improve measurement as compared to earlier transverse mass observables. We also analyze the modified phase space arising due to the constraint used in the new observable and also comment on the full event reconstruction of semi-invisible events. Subsequently, in chapter 4, we discuss the semi-invisible tau pair event reconstruction using the new observable M_{2Cons}. The efficiency of M_{2Cons} to reconstruct this semi-invisible events is compared with the older methods and a significant improvement can be noticed. Finally, in chapter 5 we summarize and conclude.

Chapter 2

Effect of partial topology information on inclusive variable $\hat{s}$

In this chapter we briefly describe the global and inclusive variable $\sqrt{\hat{s}_{min}}$ and its sisters which are important to our analysis. But before that we mention about the event topology and notation which would be followed throughout this thesis. We categorize the topology that can be produced at the LHC, in the context of SM as well as BSM theories. The topologies are as follows:

- ◇ *Antler topology*, in which a heavy resonance produced at the LHC and subsequently decays to visible and invisible particles, realized in different SM processes and a variety of new physics models, is very common and widely explored. The SM Higgs boson decaying semi-invisibly through the W-boson,[1] $h \to W + W^* \to \ell\nu + \ell\nu$, or via τ lepton, $h \to \tau + \tau \to W^*\nu_\tau + W^*\nu_\tau$, are some significant channels in the context of the SM Higgs search at the LHC. Similarly, in several BSM theories, the search strategy relies on antler topology. Some of these include the heavy Higgs of supersymmetry (SUSY) decaying to the Z-boson and the lightest supersymmetric particle (LSP) via neutralinos, $H \to \tilde{\chi}_2^0 + \tilde{\chi}_2^0 \to Z\tilde{\chi}_1^0 + Z\tilde{\chi}_1^0$ [71] and the SUSY extended Z' decaying to the lepton and the LSP via the slepton, $Z' \to \tilde{\ell}^+ + \tilde{\ell}^- \to \ell^+\tilde{\chi}_1^0 + \ell^-\tilde{\chi}_1^0$ [72, 73]. Similarly, in a universal extra-dimensional

[1]Note that except for the fact that $h \to W + W^*$ probably signifies the most familiar SM antler channel, this off-shell production of W is not pursued further in the present analysis.

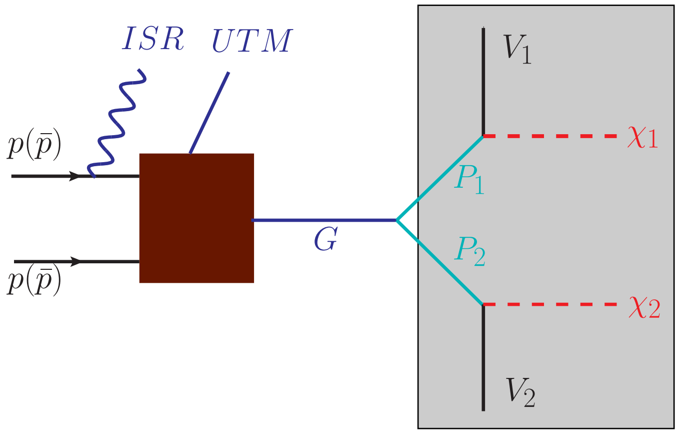

Figure 2.1: Archetype of antler topology where G, a heavy resonance particle with mass m_G produced at hadron collider, decays to two daughter particles P_1 and P_2 through two-body decay, each of which subsequently decays to produce SM visible particle (V_i) and an invisible or dark matter particle (χ_i). This topology can be considered for SM Higgs production with subsequent decays into visible SM particles and massless neutrinos as invisibles. On the other hand, in a BSM scenario, G (a parity-even state) can decay to produce (parity-odd states) P_i and χ_i. To keep this production topology general, we keep initial state radiation (ISR) emitted by the initial partons and upstream transverse momentum (UTM) coming from particle produced in hard scattering associated with the heavy resonance G.

model, second excitation states can decay to first excitation states, $Z^{(2)} \to L^{(1)} + L^{(1)} \to \ell^- \gamma^{(1)} + \ell^+ \gamma^{(1)}$ [74, 75]. The semi-invisible decay of doubly charged exotic scalars in many BSM scenarios can produce SM particles via W pairs, $\phi^{++} \to W^+ + W^+ \to \ell^+ \nu_\ell + \ell^+ \nu_\ell$ [76]. Moreover, the heavy Higgs or heavy Z' can also decay semi-invisibly to SM particles via $t\bar{t}$ pairs, $H/Z' \to t + \bar{t} \to bW^+ + \bar{b}W^- \to b\ell^+\nu_\ell + \bar{b}\ell^-\nu_\ell$. In addition, antler topology can also be realized at the linear collider, as the fixed center of mass (c.m.) energy is equivalent to the heavy resonance produced in its rest frame before pair production and subsequent decay (for example, see [77]).

A representative diagram for the antler topology is shown in fig. 2.1, where a parity-even[2] heavy resonance particle G (grandparent) with mass m_G decays to two parity-odd particles P_1 and P_2, each of which subsequently decays to a Standard Model particle (V_i) and an invisible or dark matter

[2]Parity is only pertinent to the BSM processes having stable invisible exotic particles in the final state.

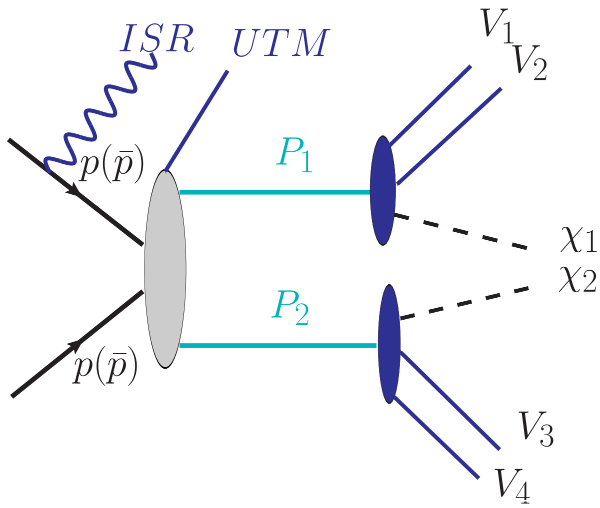

Figure 2.2: Representative for a simple non-antler topology where after production of two heavy parent particles P_α, each of them leading to a single invisible massive particle χ_j together with a number of visibles V_i in the final state. The blue blob represents an intermediate particle which may be off-shell or on-shell. The visible particles are SM particles measurable at the detector and represented by blue lines denoted by V_1, V_2, V_3 and V_4 respectively. The invisible particles are represented by black dashed lines denoted by χ_1 and χ_2 respectively.

particle (χ_i). We assign momenta to visible and DM particles on the two sides of the decay chain as p_i and q_i with $i = 1, 2$, respectively. Moreover, we denote the masses of the parents (P_i) and the invisible daughters (χ_i) as m_P and m_χ, respectively. The primary motivation of this analysis is to determine these unknown parameters. Though we have shown a generic antler topology in fig. 2.1, in this analysis we are interested in the symmetric antler process motivated by the above examples. The symmetric antler includes same parent ($P_1 = P_2$) and same daughter ($\chi_1 = \chi_2$) particles, or at least their masses are same, $m_{P_1} = m_{P_2} = m_P$ and $m_{\chi_1} = m_{\chi_2} = m_\chi$. In case of the SM, one considers nearly massless neutrino with $m_\chi = 0$.

- ◇ *Non-antler topology*, shown in fig. 2.2, is motivated by various BSM examples also abundant in SM processes. Most of the BSM theories, respecting the DM stabilizing symmetry Z_2 as discussed earlier, produce non-antler topology at the LHC. The SM top pair production with dileptonic channel involving neutrinos drives one for the consideration of non-antler topology. Similarly, BSM particles (*e.g.*, gluino, squark in supersymmetry) in dark matter motivated models are produced in pairs. As a result, the final state decay products involve two massive invisible particles (DM candidates) along with visible particles as shown in the fig. 2.2.

In the topology under consideration, two parents denoted by P_1 and P_2 are either produced in hard scattering at the hadron collider, or may have been produced from heavier particles which are part of a longer decay chain in the event. Eventually each of these parents decays to produce two visible (*e.g.*, two particles with blue lines shown in fig. 2.2) and one invisible particle. The topology can also contain intermediate particles which may be on-shell or off-shell, symbolized by the blue blob, with only the final products shown. Momenta p_j of these visible SM particles V_j $(j = 1, \ldots, 4)$ represented by blue lines can be measured by the detector. On the contrary, the invisible particles χ_i $(i = 1, 2)$ in black dashed lines are of BSM nature with individual masses m_{χ_i}, and 3-momenta q_i.

2.1 Partonic mandelstam variable: $\sqrt{\hat{s}_{min}}$

Let us start by discussing briefly the variable $\sqrt{\hat{s}}_{min}$ which was first introduced [23] to determine the mass scale associated with any generic process (or event topology) involving missing particles. It is inspired by the fact that the precise knowledge of the partonic system CM energy $\sqrt{\hat{s}}$ carries kinematic information like masses of heavy resonance, or threshold of pair production at the hadron collider. Hence, one may like to know the distribution of this variable even approximately, after recognizing the fact that there is no way we can completely reconstruct the event, or extract all the momentum information in case of general semi-invisible production at the hadron collider. Utilizing all the experimentally observed quantities, the best one can devise is the minimum partonic CM energy which is compatible (or consistent) with the observed visible momenta and missing transverse momentum. Although general event topology can have a wide diversity in the production mechanism of visibles and invisibles and also in their number, it emerged that the final minimization leads to a rather simple and versatile functional form for $\sqrt{\hat{s}}_{min}$.

This variable was further extended [24] to apply in general subsystems, and also utilized reconstructed events to safe guard the generic variables from underlying events and ISR [78, 79]. Subsequently, these $\sqrt{\hat{s}}$ variables were shown and classified [19, 80] as M_1 type of mass-bound variables[3] represented in a compact nomenclature of $M_{...}$ class of variables.

One can simplify the discussion under the following assumptions which are rather common in a wide class of BSM models: (i) The DM stabilization is achieved by discrete Z_2 symmetry. As a result, all BSM particles in the theory would be produced in pairs leading to two stable DM particles in the final state. They stay invisible in the detector resulting in missing transverse energy as their combined footprint. (ii) There is only one DM candidate in the theory, or if there are multiple DM particles, then they are degenerate in mass. One can note that even after making these two assumption the variable $\hat{s}_{min}$ remains global and inclusive.

Under these assumptions the analytic expression and properties of this mass-bound variable $\sqrt{\hat{s}}_{min}$ can be discussed using the non-antler topology displayed[4] in fig. 2.2. The partonic Mandelstam variable for this topology is given by,

$$\hat{s} = \left(E^v + \sum_{i=1}^{n_{inv}} \sqrt{m_i^2 + \vec{q}_{iT}^{\,2} + q_{iz}^2} \right)^2 - \left(P_z^v + \sum_{i=1}^{n_{inv}} q_{iz} \right)^2 . \tag{2.1}$$

Here, $n_{inv} = 2$, is the number of invisible particles, $E^v = \sum_j e_j^v$ and $P_z^v = \sum_j p_j^z$ are total energy and total longitudinal component of the visible momenta. In the above equation, missing transverse momentum constraints $\vec{\not{P}}_T = \sum_i \vec{q}_{iT}$ are also taken into account. Clearly, even in this simplified case, there are $3n_{inv} = 6$ unknown momentum components, as well as unknown invisible mass with only

[3] A Wide variety within these classes is constructed systematically considering different projection methods, additional second projection [61, 68], and considering different orders of the operations. Interestingly, most of the existing mass variables devised based on their differing utility can be accommodated in this unified picture, leaving many more new variable elements in this class hitherto unexplored.

[4] In general, there can be any number of visibles including asymmetric production topology or asymmetric invisibles (*e.g.*, as in [63]) in the final state, but here we restrict our discussion to symmetric pair production for simplicity. The most generic representation is discussed in the ref. [23] in which these $\sqrt{\hat{s}}$ variables are constructed.

two constraints from missing transverse momentum. So one cannot hope to calculate true values of $\hat{s}$ event by event. But it is important to realize that there is an absolute minimum exists for $\hat{s}$ in each event which also satisfies all these constraints. By minimizing $\hat{s}$ with respect to unknown momenta $\vec{q}_i$ subject to the missing transverse momenta $\vec{\not{P}}_T$ constraints one gets

$$\vec{q}_{iT} = f_m^{(i)} \, \vec{\not{P}}_T \, , \tag{2.2}$$

$$q_{iz} = f_m^{(i)} \frac{P_z^v}{\sqrt{(E^v)^2 - (P_z^v)^2}} \sqrt{M_{inv}^2 + \vec{\not{P}}_T^2} \, , \tag{2.3}$$

where $f_m^{(i)}$ is a dimensionless mass fraction, which varies between 0 and 1 and is given by $f_m^{(i)} = \frac{m_i}{M_{inv}}$ and $M_{inv} = \sum_{i=1}^{n_{inv}} m_i$ is the total sum of all invisible masses. Now replacing the above expression for $\vec{q}_{iT}$ and q_{iz} in eq. 2.1 one gets the final form of $\hat{s}_{min}$ as

$$\sqrt{\hat{s}_{min}(M_{inv})} = \sqrt{(E^v)^2 - (P_z^v)^2} + \sqrt{\vec{\not{P}}_T^2 + M_{inv}^2}. \tag{2.4}$$

One can notice that the $\hat{s}_{min}(M_{inv})$ involves all the measured quantities except the mass parameter M_{inv}. Evidently eq. 2.4 is a very simple and elegant formula which can be used for any topology. Once we have calculated $\hat{s}_{min}$, although as function of M_{inv}, the next task is to find out whether it gives any new information about the mass scale of new physics. Interestingly, the peak of the $\hat{s}_{min}$ is correlated with the mass scale of new physics subject to the correct input of M_{inv} as,

$$(\sqrt{\hat{s}_{min}(M_{inv})})^{peak} \approx (\sqrt{\hat{s}})^{thr}, \tag{2.5}$$

where $(\sqrt{\hat{s}})^{thr}$ is the threshold of pair production or mass of heavy resonance for single production. Hence, by measuring the peak location one can determine the mass scale of new physics produced at LHC.

One can follow from the computation that the $\hat{s}_{min}$ does not assume any particular event topology or the DM stabilizing symmetry of the model. Based on common BSM scenarios, we restrict our description (also in fig. 2.2) assuming Z_2 symmetry, so that, pair production of BSM particles results in two invisible massive particles in the final state. From minimization conditions in eqs. 2.2 and 2.3 one can infer that each DM particle carries a fraction of missing momenta, proportional to the corresponding mass fraction $f_m^{(i)}$. However, the final $\hat{s}_{min}$ is simply a function of total M_{inv} irrespective to this fraction. Once we assume a pair of invisibles in the final state with the same mass (or both massless), then this fraction $f_m^{(i)}$ comes out as 1/2 for any choice of trial mass[5] including the true invisible mass. The invisible momenta after the minimization are,

$$\vec{q}_{iT} = \frac{1}{2}\,\vec{\not{P}}_T, \tag{2.6}$$

$$q_{iz} = \frac{1}{2}\frac{P_z^v}{\sqrt{(E^v)^2-(P_z^v)^2}}\sqrt{M_{inv}^2+\vec{\not{P}}_T^2}. \tag{2.7}$$

These invisible momenta, calculated from the minimum, may not represent exactly those of the true event. However, the uniqueness of these momenta can be useful to study the semi-invisible decays involved both in the SM and BSM scenarios. Momentum reconstruction can be exploited to analyze the properties of the top quark decaying invisibly in the SM, whereas DM motivated BSM models are commonplace where uniqueness of invisible momenta can help to study decays with different topologies. One can notice that the invisible momenta constructed through $\hat{s}_{min}$ are always parallel to each other with a magnitude proportional to the mass fraction. Here we investigate how a partial knowledge of event information can improve the variable $\hat{s}_{min}$ and also the reconstructed momentum obtained from it. In our further discussion, we divide the production topology in two types, viz., antler topology and non-antler topology. We discuss $\hat{s}_{min}$ with and without putting on-shell constraints in both kinds of topologies.

[5] Although, the mass fraction $f_m^{(i)}$ appears to be singular for a choice of zero invisible masses, one can recalculate starting with a massless scenario and minimize to get the fraction $f_m^{(i)} = \frac{1}{2}$. Alternatively, from this present expression with arbitrary masses, one can first use the equality of unknown invisible masses before setting it to zero to get back the same fraction.

2.2 $\sqrt{\hat{s}_{min}}$ with ISR/UTM

The $\hat{s}_{min}$ being a global and inclusive variable with many interesting properties is not protected from the effect of initial state radiation (ISR), multi-parton interaction (MPI) and upstream transverse momenta (UTM). In other words the most useful property of this variable that its peak is correlated with the new physics mass scale is no longer valid once the above inevitable effects are included. Some methods are proposed in the literature to rescue the $\sqrt{\hat{s}_{min}}$ variable keeping all its interesting properties intact, which we discuss below.

It was noticed in ref. [23] that the contribution of ISR/MPI on $\sqrt{\hat{s}_{min}}$ most likely comes from the forward region with large $|\eta|$ values. Hence, a suitable cut on η, $|\eta| < \eta_{max}$, may reduce these adverse effects. Since there is no theoretical motivation for choosing the appropriate value of η_{max}, this approach introduces an uncontrollable systematic error. In addition, this procedure is model dependent because the ISR effect depends on various factors like collider energy, mass of new resonant particle and initial partons before collision etc.

Subsequently, it was proposed that the effect of ISR on the $\hat{s}_{min}$ can be calculated along with contribution from QCD [78, 79]. The analytical formula of $\hat{s}_{min}$ as given in eqn. 2.4 can be equivalently written as

$$\sqrt{\hat{s}_{min}(M_{inv})} = \sqrt{(M_v)^2 + \vec{\not{P}}_T^2} + \sqrt{\vec{\not{P}}_T^2 + M_{inv}^2}, \tag{2.8}$$

where M_v is the total visible particle invariant mass. It is argued that the second term in the eq. 2.8 is mildly affected by the ISR. It is the total visible invariant mass M_v which is affected strongly by the ISR and is responsible for shifting the peak of the $\hat{s}_{min}$ distribution. In refs. [78, 79], the shift in M_v due to ISR is calculated using QCD from first principles and thereby the movement in $\hat{s}_{min}$ distribution peak position is measured. Hence, this method allows a way to handle the ISR in the calculation of $\hat{s}_{min}$ and mass scale of new physics without accounting for the MPI and UTM effects.

- **$\hat{s}_{min}^{reco}$ method**

This method does not modify definition of the $\hat{s}_{min}$. Rather, it modifies the observable quantities (E, $\vec{P}$ and $\vec{\not{P}}_T$) that go into it. The definition of $\hat{s}_{min}$ as in eq. 2.4 uses the total visible energy and momentum observed in the calorimeter, whereas the present method proposes to use the total energy and momentum from the reconstructed objects, like jets, photons, electrons and muons etc.

$$\sqrt{\hat{s}^{reco}_{min}(M_{inv})} = \sqrt{(E^v_{reco})^2 - (P^v_{z(reco)})^2} + \sqrt{\vec{\not{P}}^{\,2}_{T(reco)} + M^2_{inv}}, \tag{2.9}$$

with

$$E^v_{reco} = \sum_{i=1}^{n} E_i, \tag{2.10}$$

$$\vec{P}^v_{reco} = \sum_{i=1}^{n} \vec{P}_i, \tag{2.11}$$

$$\vec{\not{P}}_{T(reco)} = -\vec{P}_{T(reco)}, \tag{2.12}$$

where n is the number of reconstructed objects. This approach definitely outperforms the $\hat{s}_{min}$ method in measuring the hard scattering scale (*i.e.*, new physics energy scale) because by employing reconstructed objects the additional calorimeter energy is removed. But this method also does not solve the underlying event problem completely, since there can be an ISR hard jet which will be counted as reconstructed jet and results in increasing in the value of $\hat{s}^{reco}_{min}$ even though the peak location remains the same.

- $\hat{s}^{sub}_{min}$ **method**

A general topology can be divided into two parts, first, the hard scattering (HS) part and second, the underlying event part (ISR, UTM). We are mainly interested in knowing the energy scale associated with the HS part. This method defines a subsystem of the topology which only includes the HS part. In a scenario when one can identify the subsystem unequivocally, it is possible to redefine the $\hat{s}_{min}$ for the interested subsystem. One more crucial assumption associated with this approach is that no invisible particles originated from ISR/UTM. The subsystem

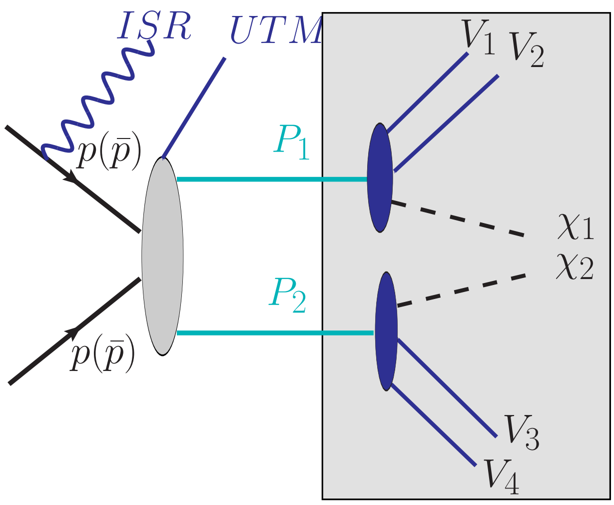

Figure 2.3: Representative for a simple non-antler topology where after production of two heavy parent particles P_α, each of them leading to single invisible massive particle χ_j together with number of visibles V_i in the final state. The blue blob represents the intermediate particle which may be off-shell or on-shell. The visible particles are SM particles measurable at the detector and represented by blue lines denoted by V_1, V_2, V_3 and V_4, respectively. The invisible particles are represented by black dashed lines denoted by χ_1 and χ_2, respectively. Subsystem of the topology is represented by the gray shaded region which includes the HS part only.

is shown in fig 2.3 by the gray shaded region. The rest of the figure is exactly the same as fig 2.2 where UTM can include all additional visible particles from the earlier part of the decay chain. The observable quantities are divided into two parts as follows,

$$E^v = E^v_{sub} + E^v_{ue}, \tag{2.13}$$

$$\vec{P}^v = \vec{P}^v_{sub} + \vec{P}^v_{ue}, \tag{2.14}$$

$$\vec{\not{P}}_T = -\vec{P}_{T(sub)} - \vec{P}_{T(ue)}, \tag{2.15}$$

where E^v_{sub} and $\vec{P}^v_{sub}$ are total energy and momentum of the subsystem, respectively. Similarly, E^v_{ue} and $\vec{P}^v_{ue}$ are the total energy and momentum of the underlying event, respectively. The minimum subsystem partonic Mandelstam variable, $\hat{s}^{sub}_{min}$, consistent with the above measurements shown in eqs. 2.13- 2.15 is

$$\sqrt{\hat{s}^{sub}_{min}} = \sqrt{\left(\sqrt{(E^v_{sub})^2 - (P^v_{z(sub)})^2} + \sqrt{\vec{\not{P}}_T^{\,2} + M^2_{inv}}\right)^2 - P^2_{T(ue)}}. \tag{2.16}$$

Now correlation between the location of the peak of the $\sqrt{\hat{s}^{sub}_{min}}$ distribution which is a function of the invisible mass parameter, M_{inv}, and the mass scale of the subsystem (or the hard scattering) is restored. This approach works because one can identify all the visible particles from the subsystem.

2.3 Constrained variable $\hat{s}$ for antler topology

A representative diagram for antler topology is shown in fig. 2.1. A parity even heavy resonant state G, produced through on-shell production at the hadron collider, promptly decays to a pair of parity odd particles P_1 and P_2. In this simplified picture, each P subsequently decays in the same way as described earlier in fig. 2.2, and thus produces a couple of visible particles with an invisible daughter particle. We also keep the same notation for the momentum assignment associated to all final particles. Before defining $\hat{s}_{min}$ in the presence of the additional constraints, we first list all the constraints available for this present topology. Apart from the antler resonance mass-shell constraint at some fixed value of the $\hat{s}$ depending upon the resonant mass m_G,

$$(\sum_j p_j + \sum_i q_i)^2 = m^2_G = \hat{s}^{True}. \tag{2.17}$$

Additional mass equations and missing transverse momentum relations for this topology can be put together as, $\{constraints\}$:

$$(p_1 + p_2 + q_1)^2 = m^2_{P_1},\ (p_3 + p_4 + q_2)^2 = m^2_{P_2}\,, \tag{2.18}$$

$$q_1^2 = m^2_{\chi_1},\ q_2^2 = m^2_{\chi_2}\,, \tag{2.19}$$

$$\vec{q}_{1T} + \vec{q}_{2T} = \vec{\not{P}}_T. \tag{2.20}$$

$\{m_{P_1}, m_{P_2}\}$ and $\{m_{\chi_1}, m_{\chi_2}\}$ are the masses[6] of the intermediate particles $\{P_1, P_2\}$ and the invisible particles $\{\chi_1, \chi_2\}$ respectively. Clearly, using the above constraints in eqs. 2.18-2.20 one can reduce the number of free parameter to two. Afterwards, in Sec. 2.5, we will further demonstrate the constrained regions in this parameter space. One can also notice that in the eqs. 2.18 the ordering of the particles in a particular decay chain does not affect the constraints but assigning particles to the decay chain does. The combinatorial ambiguity of the latter type is severe when one has a long decay chain which is absent in our analysis. In general, this type of problem can be partially controlled using existing methods like the hemisphere method [35] and the P_T v. M method [32].

Now we are in a position to formulate a new variable, dubbed $\hat{s}^{cons}_{min}$, defined as the minimum partonic Mandelstam variable which satisfies all the above *constraints* in the event,

$$\hat{s}^{cons}_{min} = \underset{\{constraints\}}{min_{\vec{q_1},\vec{q_2}}} [\hat{s}(\vec{q_1},\vec{q_2})]. \tag{2.21}$$

Among all the constraints defined in the eqs. 2.18-2.20, the variable $\hat{s}_{min}$ already satisfies the last four constraints consisting of two missing $\vec{\not{P}}_T$ components and two mass-shell constraints from invisible daughters. In other words, new variables are further constrained with mass-shell relations of intermediate parents.

The true value of the partonic Mandelstam variable for an antler topology is the mass of the heavy resonance, that is $\sqrt{\hat{s}^{True}} = m_G$, once the heavy resonance is produced on-shell and has narrow decay width. Hence, any mass bound variable constructed by minimization, such as, $\hat{s}_{min}$ for antler topology, needs to be bounded from above satisfying the relation $\hat{s}_{min} \leq \hat{s}^{True}$. This end point can be measured from the endpoint in a distribution over many events. The constrained variable $\hat{s}^{cons}_{min}$ also satisfies a similar relation $\hat{s}^{cons}_{min} \leq \hat{s}^{True}$, having endpoint at

[6]Note that throughout the analysis we have assumed the both the intermediate and daughter masses are known and have used their true masses in the *constraints*. However, in a scenario when the invisible particle mass is unknown, one can go ahead with the constrained variables assuming some trial masses $(\tilde{m}_{\chi_1}, \tilde{m}_{\chi_2})$ in eqs. 2.19. One can then expect a correlation between the trial invisible masses and the endpoints in constrained variable distributions.

$\hat{s}^{True}$. However, additional intermediate particle mass-shell constraints ensure a larger value of $\hat{s}^{cons}_{min}$ over $\hat{s}_{min}$ for each event. This inequality would also reflect in the mass variable distributions contributing larger number of events at the endpoint of the distribution.

As we discussed earlier, a rather striking consequence of these additional mass-shell constraints is that they also permit us to construct a finite upper mass bound variable, which is meaningless otherwise. We define this constrained variable $\hat{s}^{cons}_{max}$ as the maximum partonic Mandelstam variable,

$$\hat{s}^{cons}_{max} = \max_{\substack{\vec{q_1},\vec{q_2} \\ \{constraints\}}} [\hat{s}(\vec{q_1}, \vec{q_2})], \tag{2.22}$$

satisfying all the available *constraints* in the event listed in eqs. 2.18-2.20, which, in turn, is the maximum of the physically allowed region. Since $\hat{s}^{True}$ satisfies all the available constraints in the event, it must remain within this region. Now, by definition, $\hat{s}^{cons}_{max}$ is where $\hat{s}$ is maximum inside this region and $\hat{s}^{cons}_{min}$ is where it is minimum. So, $\hat{s}^{True}$ can maximally reach up to $\hat{s}^{cons}_{max}$. Hence, $\hat{s}^{cons}_{max}$ has a lower bound at the $\hat{s}^{True}$, significantly with large number of events at this threshold. An interesting point about these reconstructed momenta from the constrained $\hat{s}$ variables minimization (maximization) is that not only are they unique, but they also improve over the momenta calculated through $\hat{s}_{min}$. In case of $\hat{s}^{cons}_{min}$, better momentum reconstruction is ensured by the points closer to its endpoint. Similarly, $\hat{s}^{cons}_{max}$ gives better reconstruction from the points associated with its threshold. These points will be discussed further in the Sec. 2.5, where these correlations will be more evident. Finally, the definitions of different $\hat{s}$ variables, after imposing different constrains, ensures the hierarchy among these mass variables:

$$\hat{s}_{min} \leq \hat{s}^{cons}_{min} \leq \hat{s}^{True} \leq \hat{s}^{cons}_{max}. \tag{2.23}$$

To illustrate the properties of these constraint variables, first we consider a simple example of SM Higgs production through gluon fusion at the hadron collider. Higgs boson decays further semi-invisibly through tau pair production, $h \to \tau\tau \to W\nu_\tau W\nu_\tau$. To compare with the representative diagram for antler

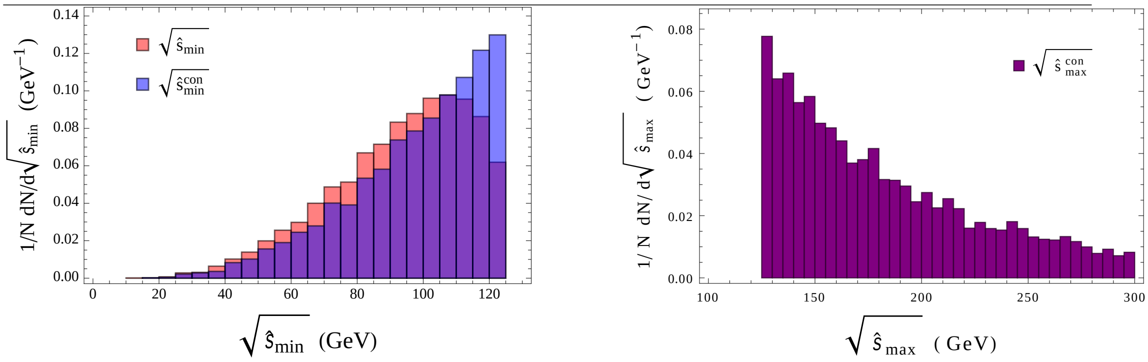

Figure 2.4: (Left) panel the distribution of $\sqrt{\hat{s}_{min}}$ and $\sqrt{\hat{s}^{cons}_{min}}$ with $\sqrt{\hat{s}^{True}} = M_h = 125.0$ GeV. The red colored histogram is for analytical formula of $\sqrt{\hat{s}_{min}}$ which also can be verified using numerical minimization, blue colored histogram is $\sqrt{\hat{s}^{cons}_{min}}$ calculated using numerical minimization. The variables $\sqrt{\hat{s}_{min}}$ and $\sqrt{\hat{s}^{cons}_{min}}$ have endpoint at the heavy resonance mass M_h but $\sqrt{\hat{s}^{cons}_{min}}$ have larger number of events because of the extra constraints it uses in its minimization. In the (Right) panel the distribution of the $\sqrt{\hat{s}^{cons}_{max}}$. As one can see it has a threshold at the true mass of the heavy resonance $M_h = 125.0$ GeV. Evidently, the $\sqrt{\hat{s}^{cons}_{max}}$ always greater than or equal to $\sqrt{\hat{s}^{True}}$. Similar unconstrained variable *i.e.*, $\sqrt{\hat{s}_{max}}$ is not present because the unconstrained phase space does not have an upper bound.

production in fig. 2.1, τ is the intermediate particle B_i, for which additional mass-shell condition is used in the minimization (maximization) of constrained $\hat{s}$. The neutrino ν_τ is the invisible particle χ_i. We considered hadronic (leptonic) decay mode for the W boson which results in two invisibles (four invisibles tested in next example) in the final state. The distributions of $\hat{s}_{min}$ and $\hat{s}^{cons}_{min}$ are shown in the fig. 2.4(left). The red binned histogram shows the distribution for $\hat{s}_{min}$, which can be calculated numerically or using an analytical expression. The blue histogram shows the distribution of constrained $\hat{s}^{cons}_{min}$. As expected, the endpoints of both the $\hat{s}_{min}$ and $\hat{s}^{cons}_{min}$ distributions are at $\sqrt{\hat{s}^{True}} = M_h = 125\ GeV$ for a choice of vanishing invisible mass. Evidently, larger number of events at the endpoint for the $\hat{s}^{cons}_{min}$ distribution with a sharper drop can be measured more precisely. This is even more important once the corresponding background is also considered together. The fig. 2.4(right) demonstrates the distribution of the other constraint variable $\hat{s}^{cons}_{max}$ which has a threshold at $\hat{s}^{True}$ with considerable number of events at the threshold.

It is expected that the endpoint of the kinematic distribution would be less

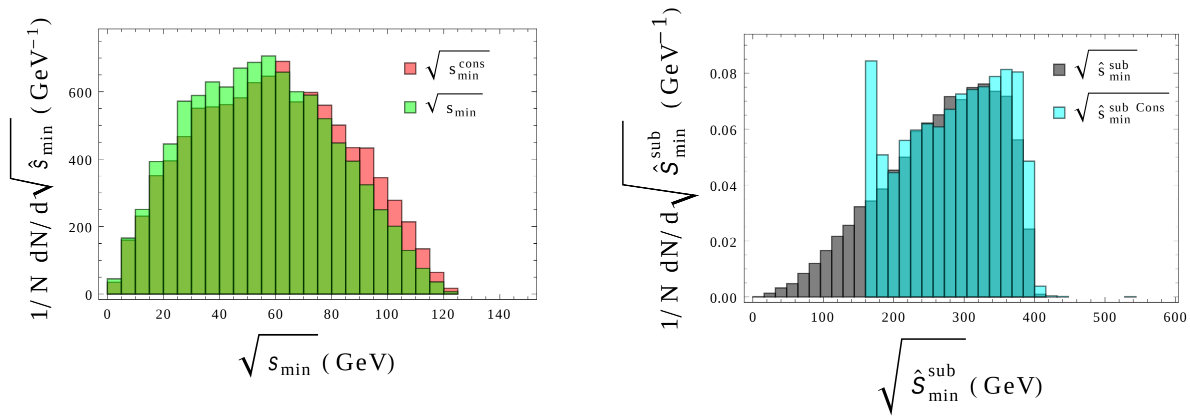

Figure 2.5: (Left) In this figure we have shown the distribution of the $\sqrt{\hat{s}_{min}}$ and $\sqrt{\hat{s}^{cons}_{min}}$ for four invisible particles in the final state. The red histogram shows the distribution of $\sqrt{\hat{s}^{cons}_{min}}$ and the green histogram shows the distribution $\sqrt{\hat{s}_{min}}$. As one can see, though there are endpoint features for both the variables, the number of events is very small and the improvement for $\sqrt{\hat{s}^{cons}_{min}}$ over $\sqrt{\hat{s}_{min}}$ is also very little. (Right) Here the black histogram is for $\sqrt{\hat{s}^{sub}_{min}}$ calculated using the analytical formula and the cyan histogram is for $\sqrt{\hat{s}^{sub,cons}_{min}}$ calculated numerically. The variables $\sqrt{\hat{s}^{sub}_{min}}$ and $\sqrt{\hat{s}^{sub,cons}_{min}}$ have endpoint at $\sqrt{\hat{s}^{sub,True}} = M_{\phi^{++}}$.

populated if one had more number of invisible particles in the event. This is because increasing the number of invisible particles would increase the number of unknown momenta restricted with the same constraints. Following our previous example, we now consider four invisible particles by decaying both W's leptonically and demonstrate the corresponding $\sqrt{\hat{s}_{min}}$ and $\sqrt{\hat{s}^{cons}_{min}}$ distributions in fig. 2.5(left). The red histogram shows the distribution for $\sqrt{\hat{s}^{cons}_{min}}$, whereas the green binned histogram shows $\sqrt{\hat{s}_{min}}$ to compare the effect due to the extra constraints. These distributions confirm that the number of events at the endpoint are considerably low as one increases the number of invisible particles in the final state. Although constrained variable can improve the situation only slightly, overall both of these distributions form a narrow tail rather than the sharp endpoint.

We further study one more interesting example from the resonant production of exotic doubly charged scalar [76] production at the hadron collider followed by its decay into the dominant decay channel producing pair of W's, which in turn decays leptonically. Hence, the resonant sub-system under consideration is $\phi^{++} \to W^+W^+ \to \ell^+\nu_\ell\ell^+\nu_\ell$. At a hadron collider this exotic state ϕ^{++} can be produced associated with charged W^- which mainly decays hadronically and it is possible to disentangle this from the antler subsystem producing a lepton pair from the exotic decay. We choose to use the corresponding subsystem variable $\sqrt{\hat{s}^{sub}_{min}}$ for our analysis. Here analytical expressions for the invisible particle momenta remain the same except the modified form for $\vec{\not{P}}_T$ which includes the visible contribution from non-sub-system [24]. The distributions for the $\sqrt{\hat{s}^{sub}_{min}}$ and the constrained variable $\sqrt{\hat{s}^{sub,cons}_{min}}$ are demonstrated in fig. 2.5(right). The dark binned histogram represents the distribution for $\sqrt{\hat{s}^{sub}_{min}}$ which can be calculated either analytically or using numerical minimization. The cyan histogram is the distribution for $\sqrt{\hat{s}^{sub,cons}_{min}}$ utilizing extra W mass-shell constraints, and minimized numerically. One can note that the $\sqrt{\hat{s}^{sub,cons}_{min}}$ performs better in getting the endpoint at the ϕ^{++} mass. The observed small tail is because of finite width from ϕ^{++} and these extra constraints ensures that the $\sqrt{\hat{s}^{sub,cons}_{min}}$ distribution starts from a threshold at $2m_W$.

2.4 Constrained variable $\hat{s}$ for non-antler topology

Non-antler topology is extremely common in most of the BSM theories and also abundant in the SM. This topology is already described in the fig. 2.2, where P_i are the parent particles produced in pair. After a cascade decay, each side of the decay chain produces a number of visibles along with a massive invisible particle χ_i. Detailed study on the behavior of $\sqrt{\hat{s}_{min}}$ as a mass bound variable has been done extensively for this kind of topology. Here we will illustrate the constrained variables in the light of additional on-shell constraints. Rather than using these exact on-shell constraints for the parent mass, which is primarily what one would like to know through these mass bound variables, ref. [70] uses constraints from

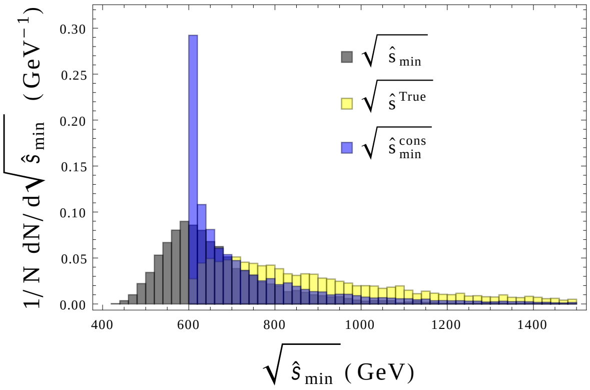

Figure 2.6: The distribution of $\sqrt{\hat{s}_{min}}$ (black) and $\sqrt{\hat{s}^{cons}_{min}}$ (blue) considering a toy model of non-antler pair production at the hadron collider is shown, with parent and invisible masses as 300 GeV and 200 GeV, respectively. Non-antler heavy-parent particle pair production must have a true parton level CM energy distribution starting from a threshold value of total parent mass as shown by the yellow histogram. As a consequence of additional constraints, $\sqrt{\hat{s}^{cons}_{min}}$ distribution also possesses this same threshold, however with a considerable number of events at the threshold.

the equality of the two parent masses. Following our analysis in the previous section, we continue using these mass-shell constraints with the expectation of improved momentum reconstruction.

As a consequence of on-shell constraints, one can expect that the $\sqrt{\hat{s}^{cons}_{min}}$ distribution would start from a threshold at the sum of the parent masses. This is contrary to the unconstrained $\sqrt{\hat{s}_{min}}$ distribution which exhibits a peak at that position giving an excellent correlation for the new physics mass scale. This is demonstrated in fig. 2.6 where distributions for $\sqrt{\hat{s}_{min}}$ (black) and $\sqrt{\hat{s}^{cons}_{min}}$ (blue) are plotted using a toy model of non-antler pair production at the hadron collider, with parent and invisible masses as 300 GeV and 200 GeV, respectively. Unlike antler decay topology where heavy-particle resonant production forms a near delta function at the parton level center of mass energy, here the heavy-parent particle pair production has a distribution starting from a threshold value of the total parent mass as shown by the yellow histogram. As we note that the $\sqrt{\hat{s}^{cons}_{min}}$ distribution also possesses this same threshold, however with a considerable number of events at the threshold. We will pursue this further in the next

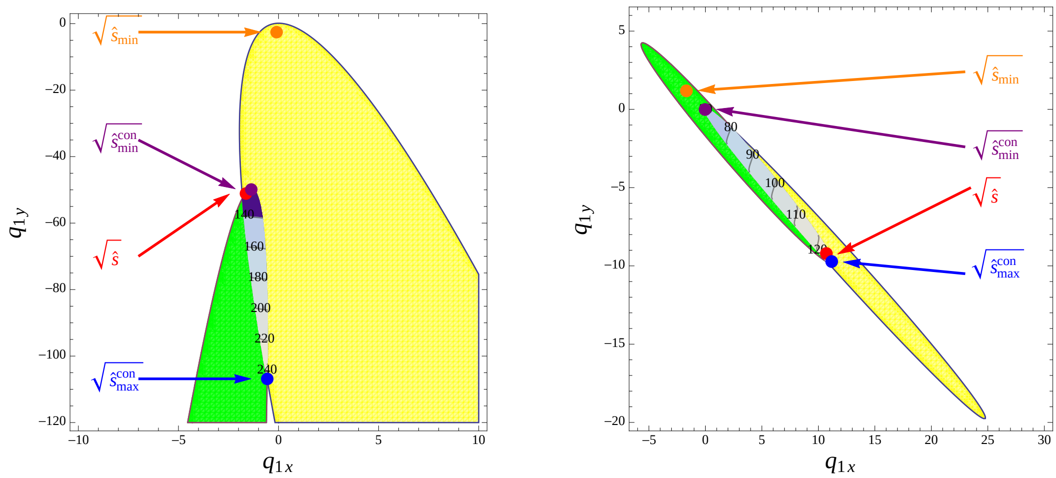

Figure 2.7: Some example events demonstrating the invisible momentum reconstruction in case of antler topology through minimization during construction of different $\sqrt{\hat{s}}$ variables. Each color shaded region is represents the phase space allowed by additional constraint in the unknown invisible momentum parameter space. In both plots the yellow elliptical region is the constrained area describing $q_{1z}(\vec{q}_{1T})$ and the green elliptical region is the constrained area for $q_{2z}(\vec{q}_{1T})$. The intersection region between these two constrained ellipses, shaded in white, is eligible for containing all the constraint $\sqrt{\hat{s}(\vec{q}_{1T})}$ parameters as well as the true $\sqrt{\hat{s}}$. Two other ends in this overlapping region would typically represent $\sqrt{\hat{s}^{cons}_{min}}$ and $\sqrt{\hat{s}^{cons}_{max}}$, with the true $\sqrt{\hat{s}}$ in between them. Since $\sqrt{\hat{s}_{min}}$ does not have this additional constraint, it would be outside the overlapping region and far from the true $\sqrt{\hat{s}}$. Inside the overlapping region $\sqrt{\hat{s}}$ contours are also presented where true c.m. energy matches with the value of the Higgs mass. The left figure shows one example event where $\sqrt{\hat{s}^{True}}$ is closer to $\sqrt{\hat{s}^{cons}_{min}}$. This event contributes at the endpoint of the $\sqrt{\hat{s}^{cons}_{min}}$ distribution and also gives better momentum reconstruction. The right figure shows another event where $\sqrt{\hat{s}^{True}}$ is close to $\sqrt{\hat{s}^{cons}_{max}}$ contributing at the threshold of this distribution with better momentum reconstruction.

section to show the improvements in the invisible momentum construction in the presence of these constraints. Analogous to the variables constructed for antler topology, one can follow a similar hierarchy among all the constrained $\sqrt{\hat{s}}$ mass variables after imposing different constraints:

$$\sqrt{\hat{s}_{min}} \leq \sqrt{\hat{s}^{cons}_{min}} \leq \sqrt{\hat{s}^{True}} \leq \sqrt{\hat{s}^{cons}_{max}}. \tag{2.24}$$

2.5 Event reconstruction capability

In this section we describe the invisible momentum reconstruction capability using mass variables $\hat{s}_{min}$ and improvement in it accounting for additional constraints in the context of antler and non-antler decay topology. Analytic expressions for invisible momenta components from the $\hat{s}_{min}$ were already discussed in Sec. 2.1. It was also argued that these reconstructed invisible momenta using $\hat{s}_{min}$ are unique irrespective of any topology considered. Note that these reconstructed momenta from the minimization of $\hat{s}_{min}$ are not the true momenta, but approximated momenta consistent with the observables in such events. These calculated momenta can be correlated with the true values to find the reconstruction efficiency similar to the other reconstruction methods like MAOS [81, 82], an event reconstruction method based on the transverse mass variable M_{T2} as discussed in chapter 4.

To describe the consequence of the constraints given in eqs. 2.18-2.19 in constructing the new variables $\hat{s}^{cons}_{min}$ and $\hat{s}^{cons}_{max}$, we reorient them to write unknown longitudinal momenta in terms of their transverse components $\vec{q}_{iT}$. We get,

$$q_{iz} = \frac{\Sigma_i P^V_{iz} \pm E^V_i \sqrt{\Sigma^2_i - (E^V_{iT} E^q_{iT})^2}}{(E^V_{iT})^2}\,, \tag{2.25}$$

with

$$\begin{aligned} \Sigma_i &= \frac{m^2_{P_1} - m^2_{\chi_i} - M^2_{vi}}{2} + \vec{P}^V_{iT}.\vec{q}_{iT}\,, && (2.26)\\ E^V_{iT} &= \sqrt{M^2_{vi} + (p^V_{iT})^2}\,, && (2.27)\\ E^q_{iT} &= \sqrt{m^2_{\chi_i} + q^2_{iT}}, && (2.28) \end{aligned}$$

where M_{vi} is the invariant mass of visibles in the i-th decay chain, $i = 1, 2$. Missing transverse momentum constraints further permit us to rewrite them in terms of single invisible particle transverse momentum components, which we choose as $\vec{q}_{1T}$ for our examples. By simplifying the right hand side of eq. 2.25, one gets the equation of an ellipse in terms of the transverse momenta and

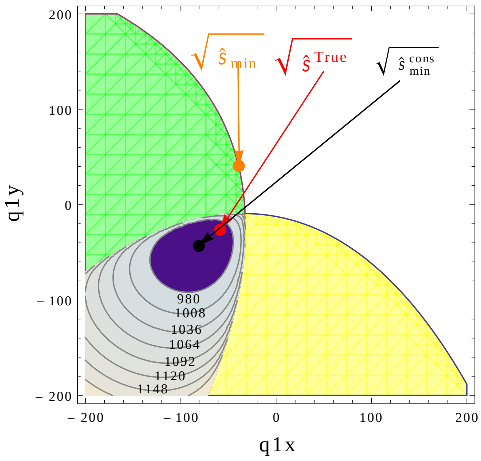

Figure 2.8: One example event demonstrating the invisible momentum reconstruction in case of non-antler topology through minimization during construction of different $\hat{s}$ variables. Description of shaded regions and mass variables are similar to previous figure.

the parameters outside the ellipse are not physical for the given event. Two elliptical allowed regions for each event correspond to two decay chains and these two regions cannot be completely disjoint from each other. All the available constraints in an event are satisfied only at the intersection region between them. Different situations can emerge for this overlapping region. Two ellipses may intersect each other over a finite region or a point (touching each other). In some cases one ellipse may contain the other ellipse.

In fig. 2.7 we consider such constrained regions demonstrated for two different events in antler topology. Each color shaded region represents the phase space allowed by the additional constraint in the unknown invisible momentum parameter space. Overlapping region between these two constrained ellipse is shaded in white where $\hat{s}$ contours are also presented. One can identify the minimum value from this intersection region as $\hat{s}^{cons}_{min}$ and the maximum value as $\hat{s}^{cons}_{max}$ which reside at opposite ends within this region. Since $\hat{s}^{True}$ also satisfies all the constraints in the event it must also remain in the intersection region and in between these two constrained points[7]. Since the $\hat{s}_{min}$ variable does not satisfy all the additional constraints in the event, it would lie outside the intersection

[7]eq. 2.25 reflects a four fold ambiguity for the longitudinal component in each event. However, the extremization of constrained $\hat{s}$ would qualify for a choice of unique momentum reconstruction.

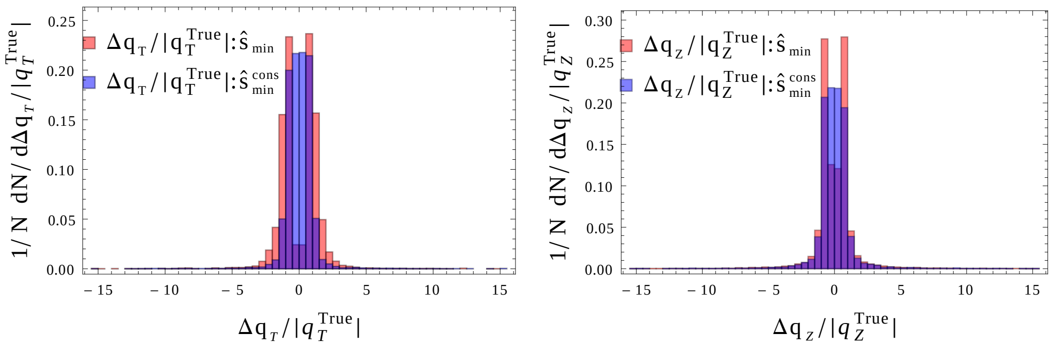

Figure 2.9: Histograms showing the distributions for deviation of the reconstructed momentum from the corresponding true momentum as a fraction of true momentum $(q_i^{reconstructed} - q_i^{true})/|q_i^{true}|$ using both unconstrained (red) and constrained (blue) $\hat{s}_{min}$ methods. Left (right) panel displays the momentum reconstruction capability in antler topology for transverse (longitudinal) components of momentum.

region and relatively far from the true value. The left figure displays one typical example event where $\hat{s}^{True}$ is closer to $\hat{s}^{cons}_{min}$. This contributes at the endpoint of the $\hat{s}^{cons}_{min}$ distribution and also gives better momentum reconstruction. The right figure shows another event where $\hat{s}^{True}$ is close to the $\hat{s}^{cons}_{max}$ contributing at the threshold of this distribution with better momentum reconstruction. In both the figures, we depicted different colored dots for the position (invisible momenta during minimization or maximization) of all $\hat{s}$ variables together with actual $\hat{s}$ correspond to that particular event. One can even read the corresponding values of these mass variables from their contours plotted within the intersection region. Similarly, in fig. 2.8 we have shown the momentum reconstruction capability of $\hat{s}^{cons}_{min}$ and $\hat{s}_{min}$ in an example of non-antler topology. The yellow and green shaded regions represent constrained $q_{1z}(\vec{q}_{1T})$ and $q_{2z}(\vec{q}_{1T})$ respectively and their intersection region is suitable for constrained $\hat{s}$. The red, orange and black points show the true momenta and reconstructed momenta given by $\hat{s}_{min}$, $\hat{s}^{cons}_{min}$ respectively.

We are now in a position to quantify the capability of momentum reconstruction. fig. 2.9 exhibits the histograms showing the distributions for deviation of the reconstructed momentum from the corresponding true momentum as a fraction of true momentum $(q_i^{reconstructed} - q_i^{true})/|q_i^{true}|$ using both unconstrained and constrained $\hat{s}_{min}$ methods. The left panel in fig. 2.9, displays the momentum reconstruction capability in an antler topology for transverse components of momentum. Similarly, the right panel, is for the corresponding longitudinal component of the momentum. In each figure, one histogram (in red bins) is shown for $\hat{s}_{min}$ which agrees with the corresponding analytical form. Also, histograms with blue bins are plotted in the same figure to display the momentum reconstruction capability using constrained minimization $\hat{s}_{min}^{cons}$ pointing out improvements over the unconstrained one.

We discussed the additional constraints in $\hat{s}_{min}$ to choose the minimization that gives reconstructed invisible momenta closer to their true values. To understand this consequence better, we look into the movements of these calculated momenta once we impose the constraints. In fig. 2.10 we demonstrate this through a correlation plot of constructed invisible momentum versus the corresponding true momentum taking few random representative event points. In both plots, each red dot point represents the calculated momentum derived from the $\hat{s}_{min}$ against the corresponding true momentum for each event. Similarly, green dots are for corresponding momentum derived from the $\hat{s}_{min}^{cons}$. The purple arrows connecting from one red dot to other green dot represent the shift in the derived momentum once extra constraints are imposed. Since the true momentum is always same for a particular event, shifts due to minimization in different mass variables are only horizontal. These arrows represent the degree of change due to constraints, shifting calculated momenta towards the diagonal true momentum points. Blue points along the diagonal simply correlate the true momenta with themselves in each event to give the perspective of how derived momenta are correlated against the true values. Left (right) plot corresponds to the transverse (longitudinal) momenta derived from $\hat{s}_{min}$ and $\hat{s}_{min}^{cons}$.

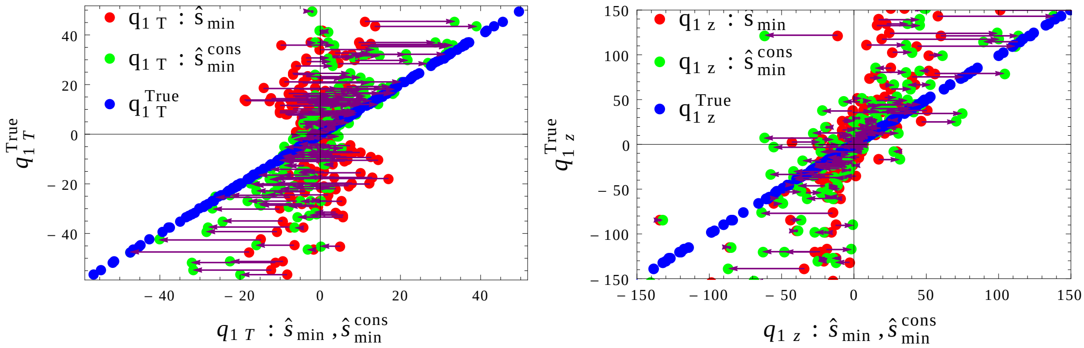

Figure 2.10: Correlation plot, taking few random representative event points, showing the shift of reconstructed transverse momenta (in left panel) and longitudinal momentum component (in right panel) derived from $\hat{s}_{min}$ and $\hat{s}^{cons}_{min}$. In both plots, each red dot represents the calculated momentum derived from $\hat{s}_{min}$ against the corresponding true momentum for each event. Similarly, green dots are for corresponding momentum derived from $\hat{s}^{cons}_{min}$. The purple arrows connecting from one red dot to a green dot represent the shift in the derived momentum once extra constraints are imposed. Blue points along the diagonal simply correlate the true momenta with themselves in each event to give the perspective of how derived momenta are correlated against the true values.

Chapter 3

Constrained M_2 variable

In this chapter we discuss the (1+2)-dimensional transverse mass variable M_{T2} and various properties associated with it. We then describe the importance of (1+3)-dimensional observable and generalize M_{T2} to its 3D analog M_2. We define a new constrained 3D mass variable M_{2Cons} for antler topology and explore all its interesting features.

3.1 Transverse mass variable: M_{T2}

We would like to address the antler topology using the mass-constraining variable for the subsystem represented by the gray shaded region shown in fig. 2.1. Let us start with the existing and popular transverse mass variable M_{T2} before moving to a generalization and finally extending to our new variable. M_{T2} is defined to have the potential to measure the masses of the BSM particles both in short or long decay chains, although its dominance and significance is mostly grounded in its capability to handle the former case. The classic definition[1] of M_{T2} is given by the larger value between two transverse masses $M_T^{(i)}$ constructed from both sides of the decay chain and minimized over unknown invisible momenta

[1] Here, "T" and "2" in M_{T2} stand for the *transverse projection* and *two parent particles*, respectively, in the topology under examination. Ref. [19] generalized and unified the concept of mass variables and set a preferred nomenclature according to the order of operations to rewrite the same variable as M_{2T} within a general M_2 family. Notably, [19] also demonstrated the fact that the transverse projection can be done using not one, but three completely different schemes.

satisfying the $\vec{\not{P}}_T$ constraints of that event. Mathematically,

$$M_{T2} \equiv \min_{\substack{\vec{q}_{iT} \\ \{\sum \vec{q}_{iT} = \vec{\not{P}}_T\}}} \left[\max_{i=1,2} \{ M_T^{(i)}(p_{iT}, q_{iT}, m_{vis(i)}; m_\chi) \} \right], \tag{3.1}$$

with the usual definition of the transverse mass for each decay chain,

$$(M_T^{(i)})^2 = m_{vis(i)}^2 + m_\chi^2 + 2(E_T^{vis(i)} E_T^{inv(i)} - \vec{p}_{iT}.\vec{q}_{iT}) \tag{3.2}$$

$$E_T^{vis(i)} = \sqrt{m_{vis(i)}^2 + p_{iT}^2}, \quad E_T^{inv(i)} = \sqrt{m_\chi^2 + q_{iT}^2} \; . \tag{3.3}$$

Here $(E_T^{vis(i)}, \vec{p}_{iT})$ and $(E_T^{inv(i)}, \vec{q}_{iT})$ are $(1+2)$-dimensional transverse energy-momenta corresponding to the visible and the invisible decay products in the i^{th} decay chain, respectively. Note that, in the definition of M_{T2}, the minimization is done over all possible partitions of $\vec{\not{P}}_T$ and the maximization of $M_T^{(i)}$ within the bracket ensures a closer shot towards the parent mass m_P. By this definition, M_{T2}, calculated for each event, must be smaller than or equal to m_P with the correct mass of invisible particle as input, shown in eqn 3.1. The equality holds when the visible and invisible particle of each decay chain are produced with equal rapidity. Hence, by measuring the endpoint of the M_{T2} distribution, mass of the parent particle can be determined with the true daughter mass as input. But the true daughter mass is also not known, so M_{T2} is calculated as a function of the trial mass hypothesis of the invisible particle, $\tilde{m}_\chi$, the true but yet unknown mass of invisible being m_χ. Mathematically, the properties of M_{T2} are

$$m_\chi \leq M_{T2}(m_\chi) \leq m_P, \tag{3.4}$$

$$\tilde{m}_\chi \leq M_{T2}(\tilde{m}_\chi). \tag{3.5}$$

The variable M_{T2} can also be measured from geometry of the topology using minimal kinematic constraints, which are parent and daughter mass shell

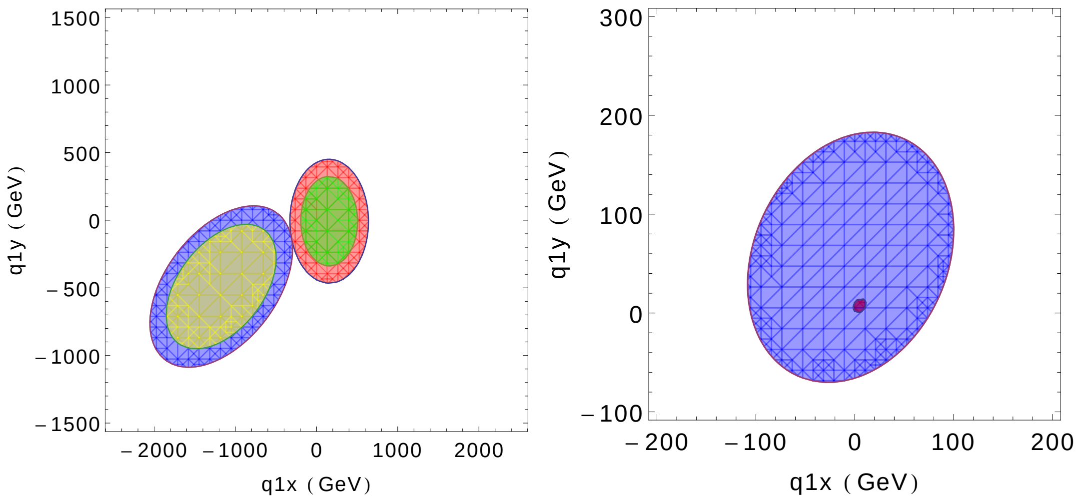

Figure 3.1: Geometrical interpretation of M_{T2} where each decay chain represents an ellipse and the ellipses are related through the missing transverse momenta constraints. The size of the ellipse are functions of unknown parent and daughter masses and increase monotonically with the parent mass. These two ellipses, for a particular choice of parent mass, are either disjoint (left) or one contains the other (right) depending on the momentum configuration. For the left panel momentum configuration, M_{T2} is determined by choosing the minimum value of the parent mass such that the two ellipses touch each other for a particular daughter mass and for the right configuration, it is the minimum value of parent mass such that one ellipse is a point contained in the other.

conditions and missing transverse momentum constraints,

$$q_1^2 = q_2^2 = \tilde{m}_\chi^2, \tag{3.6}$$

$$(p_1 + q_1)^2 = (p_2 + q_2)^2 = \tilde{m}_P^2, \tag{3.7}$$

$$q_{1T} + q_{2T} = \vec{\not{P}}_T, \tag{3.8}$$

where $\tilde{m}_P$ and $\tilde{m}_\chi$ are hypothesized parent and daughter masses. It is straightforward to show, using mass shell conditions, that each decay chain represents an ellipse. These two ellipses are not independent but are related to each other by missing transverse momenta constraints. The sizes of the ellipses are functions of the hypothesized parent and daughter masses and increase monotonically with $\tilde{m}_P$ for a particular $\tilde{m}_\chi$. These two ellipses, presupposing a parent mass, may be disjoint or one ellipse may contain the other depending on the momentum configuration of an event. For the former case, M_{T2} is the minimum $\tilde{m}_P$ such that intersection between the two ellipses is non-zero and for the latter, it is the $\tilde{m}_P$ when one ellipse becomes a point while the other one has some finite size as shown in the fig. 3.1. This approach[2] for determining M_{T2} is comparatively faster than the minimization method which is widely used, although the ideal way is to have an analytic formula which is available for certain simplified event topologies.

The analytic formula for M_{T2} assuming that the total visible transverse momenta in an event are balanced by the missing transverse momenta is given in the following,

$$(M_{T2}^{Bal}(\tilde{m}_\chi))^2 = \tilde{m}_\chi^2 + \beta_T + \sqrt{(1 + \frac{4\tilde{m}_\chi^2}{2\beta_T - (m_{vis(1)})^2 - (m_{vis(2)})^2})(\beta_T^2 - (m_{vis(1)} m_{vis(2)})^2)}, \tag{3.9}$$

with

$$\beta_T = E_T^{vis(1)} E_T^{vis(2)} + \vec{p}_{1T}.\vec{p}_{2T}, \tag{3.10}$$

where the superscript Bal in M_{T2} refers to the balanced momentum configuration. The visible and invisible particle momenta in a particular event have two kinds of momentum configuration, they are "balanced" and "unbalanced". An event is said to have balanced momentum configuration when the (1+2)-dimensional transverse mass of all decay chains are equal, else it satisfies unbalanced configuration. A detailed derivation of the above formula can be found in refs. [52, 54]. For the unbalanced configuration, the analytic formula for M_{T2}^{UnBal} is the larger value between the unconstrained minimum of the two transverse masses as follows

$$M_{T2}^{UnBal} = m_{vis(i)} + \tilde{m}_\chi. \tag{3.11}$$

The distribution of M_{T2} is shown in the left panel of fig. 3.2. As we have discussed earlier M_{T2} is a function of the trial invisible particle mass. In this

[2]Note that this approach assume the invariant mass of visible particles of each decay chain is greater than zero and sets the visible longitudinal component of momentum to zero. When the invariant mass of visible system is zero, the ellipse becomes parabola while the approach remains same, the details about general case is discussed in the ref. [83].

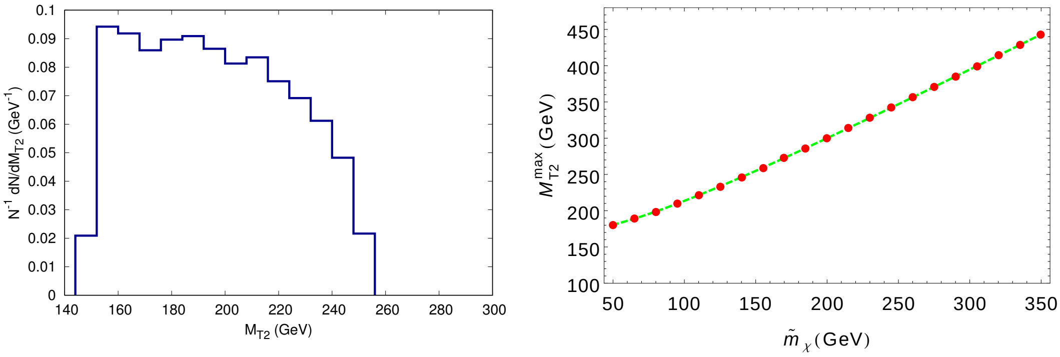

Figure 3.2: (Left) M_{T2} distribution with a value of invisible mass hypothesis less than its true value and the resulting endpoint of this distribution is not at the parent mass. M_{T2}, as evident from the eqn. 3.1, is a function of the invisible particle mass and hence the endpoint is also a function of trial invisible mass which is shown in the (right) plot. This correlation curve between M_{T2}^{max} and $\tilde{m}_\chi$ passes through the true mass point, so this relation gives a constraint between parent and daughter masses.

plot, we have taken an invisible mass hypothesis less than its true value and the resulting maximum (endpoint) is not at the parent mass, as evident from eqn. 3.4. The maximum quantity for any of these mass variables $M_{\ldots}$ (such as, M_{T2}, M_2 or M_{2Cons}) over the available data set is

$$M_{\ldots}^{max}(m_\chi) \equiv \max_{\{All\ events\}}[M_{\ldots}(m_\chi)]. \tag{3.12}$$

Now M_{T2}^{max} should provide a very close estimate of m_P with the true invisible particle mass as input, $M_{T2}^{max}(\tilde{m}_\chi = m_\chi) = m_P$. Moreover, in the scenario where the invisible particle mass is a priori unknown, *e.g.*, dark matter models, $M_{T2}^{max}(\tilde{m}_\chi)$ would still offer a useful correlation with the trial invisible mass $\tilde{m}_\chi$ as shown in the right panel of fig. 3.2. One can possess only this partial information on the unknown parent and daughter masses, unless, under *some special circumstances*, this correlation curve generates a kink feature exactly at the correct mass point.

Kink in mass measurement techniques is a widely acclaimed feature, first shown in the context of the M_{T2} variable. It was shown [53, 54] that simultaneously both parent mass m_P and daughter mass m_χ can be determined by identifying a kink in this correlation curve, where the true mass point resides. It is worthy of attention that $M_{T2}^{max}(\tilde{m}_\chi)$ has two different functional forms be-

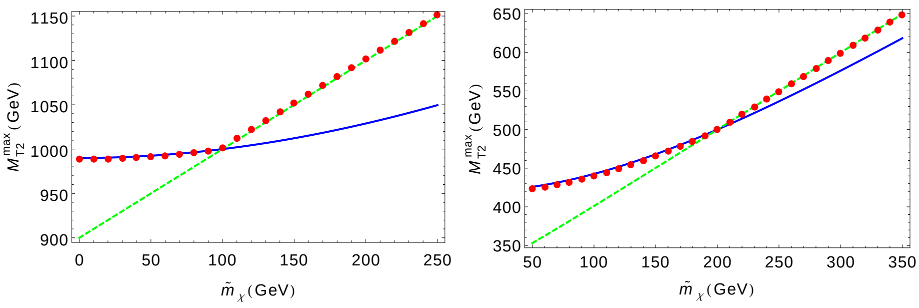

Figure 3.3: (Left) M_{T2}^{max} for the off-shell intermediate resonant particle with trial invisible mass, $\tilde{m}_\chi$, is shown. The blue line represents the function $M_{T2}^{max}(\tilde{m}_\chi)$ for $\tilde{m}_\chi < m_\chi$ while the green dashed line displays the same function for $\tilde{m}_\chi > m_\chi$. The red dotted line represents M_{T2}^{max} with the variation of $\tilde{m}_\chi$, in the full range. Similarly, the right panel displays M_{T2}^{max} for on-shell case. As we have discussed, the kink is stronger in the off-shell case compared to the on-shell case which is reflected in the plot.

fore and after this kink, and they share the same value at the true mass point. This behavior stems from the fact that the visible system invariant mass of any (or both) decay chain(s) have to have a range of values; hence, there should be at least two visible particles per decay chain. Consequently, the experimentally simpler single-step decay chain topology is deprived of such an advantage.

The visible invariant mass range of a decay chain depends on the decay topology; the maximum value attained by the invariant mass of the visible system in fig. 2.2 depends on the intermediate resonant particle, in the blue blob, produced on-shell or off-shell. Let us assume the blue blob represents a hypothetical intermediate particle which is produced off-shell, then the range of the invariant mass is

$$0 \leq m_{vis(i)} \leq m_P - m_\chi. \tag{3.13}$$

Where we have neglected the individual mass of the visible particle. The maximum of M_{T2} obtained in the frame where the two parents are produced at rest and their decay products are in transverse plane. The endpoint of M_{T2} varies with $\tilde{m}_\chi$ as,

$$M_{T2}^{max}(\tilde{m}_\chi) = \begin{cases} \alpha + \sqrt{\alpha^2 + \tilde{m}_\chi^2}, & \text{if} \quad \tilde{m}_\chi < m_\chi, \\ (m_P - m_\chi) + \tilde{m}_\chi, & \text{if} \quad \tilde{m}_\chi > m_\chi, \end{cases} \tag{3.14}$$

with

$$\alpha = \frac{m_P^2 - m_\chi^2}{2m_P}. \tag{3.15}$$

The invariant mass range, if a hypothetical intermediate resonant is produced on-shell is

$$0 \leq m_{vis(i)} \leq \sqrt{\frac{(m_P^2 - m_B^2)(m_B^2 - m_\chi^2)}{m_B^2}}, \tag{3.16}$$

where m_B is the mass of the intermediate particle. Since the minimum value is the same as in the off-shell case, $M_{T2}^{max}(\tilde{m}_\chi)$ for $\tilde{m}_\chi < m_\chi$ remains unchanged while for $\tilde{m}_\chi > m_\chi$ it will change as follows,

$$M_{T2}^{max}(\tilde{m}_\chi) = \begin{cases} \alpha + \sqrt{\alpha^2 + \tilde{m}_\chi^2}, & \text{if} \quad \tilde{m}_\chi < m_\chi \\ (\lambda + \kappa) + \sqrt{(\lambda - \kappa)^2 + \tilde{m}_\chi^2}, & \text{if} \quad \tilde{m}_\chi > m_\chi, \end{cases} \tag{3.17}$$

with

$$\lambda = \frac{m_P}{2}\left(1 - \frac{m_B^2}{m_P^2}\right) \tag{3.18}$$

$$\kappa = \frac{m_P}{2}\left(1 - \frac{m_\chi^2}{m_B^2}\right). \tag{3.19}$$

The maximum value of the invariant mass in the on-shell intermediate case is smaller in comparison to the off-shell case making the kink weaker as shown in the fig. 3.3. The left plot represents the kink in the case of an off-shell intermediate particle with the green line representing the function $M_{T2}^{max}(\tilde{m}_\chi)$ for $\tilde{m}_\chi < m_\chi$, while the red dotted line displays the same function for $\tilde{m}_\chi > m_\chi$. Similarly, the right plot portrays the kink when intermediate particle produced on-shell.

The above feature was shown where the system does not have any recoil from initial state radiation (ISR) or upstream transverse momenta (UTM). But the presence of ISR is inevitable during the production at any hadron collider. It is subsequently revealed [55, 56, 58] that a kink can also arise from a topology having a single-step decay chain on both sides, but there should be recoil to the system which may come from ISR or UTM. Both the scenarios can naturally arise in the context of a subsystem in a longer decay chain. However, sizable kink resolution only comes from events with very high recoil P_T, essentially with very low statistics.

Now to motivate the (1+3)-dimensional generalization of previous definitions as in eq. 3.1, one readily notes that M_{T2} does not utilize longitudinal components of the momenta and, thus, the available mass-shell constraints for a given topology. M_2 is thus constructed [19] out of the (1+3)-dimensional momenta by removing all "T" in the definition of eqs. 3.1-3.3 (except that of the total missing transverse momentum constraint under the curly bracket, since the longitudinal part is not available in the context of the hadron collider). Now one can apply the on-shell mass constraints in the minimization of M_2, and, depending on the constraints applied, different constrained classes of the M_2 variable (*e.g.*, M_{2xx}, M_{2cx} and M_{2cc}) can be constructed; details about these variables can be found in ref. [70]. Using similar notation, one can readily come up with the first two types of variables available from the subsystem considered in fig. 2.1. Here, M_{2cx} is the (1 + 3)-dimensional generalization of M_{T2} with the equality of the parent mass constraint applied in the minimization,

$$M_{2cx} \equiv \min_{\substack{\vec{q}_1,\vec{q}_2 \\ \left\{ \substack{\vec{q}_{1T}+\vec{q}_{2T}=\vec{P}\!\!\!/_T \\ (p_1+q_1)^2=(p_2+q_2)^2} \right\}}} \left[\max_{i=1,2} \{ M^{(i)}(p_i, q_i, m_{vis(i)}; m_\chi) \} \right], \tag{3.20}$$

with the (1 + 3)-dimensional mass from each decay chain as

$$(M^{(i)})^2 = m_{vis(i)}^2 + m_\chi^2 + 2(E^{vis(i)} E^{inv(i)} - \vec{p}_i.\vec{q}_i). \tag{3.21}$$

The corresponding M_{2xx} variable is simply realized by removing the last constraint inside bracket, just like the transverse mass case in eq. 3.1. It is straightforward to show [70] that,

$$\begin{aligned} M_{T2} &= M_{2xx} \equiv M_2 && (3.22) \\ &= M_{2cx}. && (3.23) \end{aligned}$$

Also, note that in our example, there is one visible particle per decay chain in the final state. Hence, M_{T2} and other variables always come from a balanced configuration irrespective of the choice of trial invisible mass. So once again the maximum M_{T2}^{max} (or the maxima of other variables as in eqs. 3.22 and 3.23) can only give a constraint between parent and invisible particle masses.

3.2 Constrained M_2 variable: M_{2Cons}

In the example topology under consideration, there is one visible particle, per decay chain in the final state. Hence, M_{T2} and other variables always come from a balanced configuration irrespective of the choice of trial invisible mass. So once again the maximum M_{T2}^{max} (or the maxima of other variables as in eq. 3.22 and eq. 3.23) can only give a constraint between parent and invisible particle masses.

Now, by looking at fig. 2.1, one realizes that the parents (P_1, P_2) actually originate from a heavy resonance (G). In a BSM scenario, even-parity G can directly decay to observable SM particles and hence the mass, m_G, can in principle be measured. Before we move further, we assume that in our topology only this heavy resonance mass m_G is known. We are now in a position to develop a variable using this mass constraint, so that[3]

$$M_{2Cons}(\tilde{m}_\chi) \equiv \min_{\substack{\vec{q}_1,\vec{q}_2 \\ \left\{ \substack{\vec{q}_{1T}+\vec{q}_{2T}=\not{\vec{P}}_T \\ (p_1+p_2+q_1+q_2)^2=m_G^2} \right\}}} \left[\max_{i=1,2} \{ M^{(i)}(p_i, q_i, m_{vis(i)}; \tilde{m}_\chi) \} \right], \tag{3.24}$$

where the $(1+3)$-dimensional invariant mass is $M^{(i)}$ as in eq. 3.21. Additionally, the dependence on the unknown trial invisible mass $\tilde{m}_\chi$ is shown explicitly. With this additional constraint, one expects a more squeezed phase space affecting this new variable as compared to that of M_2. Furthermore, we will soon realize that this effect is a little more far-reaching. Before we gradually move to demonstrate that, let us open the discussion with the consequences of this new variable in the invisible momentum space.

[3] One can also consider an additional constraint using the equality of parent masses $(p_1 + q_1)^2 = (p_2 + q_2)^2$ in M_{2Cons}. Although this would further constrain the allowed invisible momentum space, it would finally choose the same minima. Hence, our arguments with this present example and analysis remain the same.

The additional heavy resonance mass-shell constraint in the minimization (last condition inside bracket of eq. 3.24) constrains the invisible particle momenta, such that the invariant mass of the parents is confined to a resonance of mass m_G. This is true for each event. In fig. 3.4, the effect of this constraint is demonstrated for one event with an example where the trial invisible particle mass $\tilde{m}_\chi$ is considered smaller than the as yet unknown true mass m_χ. The region represented by the light temperature map color gradient is the maximum between two transverse masses $M_T^{(i)}$, as in eq. 3.1 before executing the minimization. This is shown with respect to the invisible momenta components, q_{1x} and q_{1y}, by taking care of the missing transverse momenta constraints. Now the minimum of this quantity, which is nothing but M_{T2}, is the minimum point in the color map displayed by the filled circle ●, and different contour lines are shown by *dashed curves*. Moving to our $(1 + 3)$-dimensional new variable with the heavy resonance mass-shell constraint in eq. 3.24, once again after doing a similar exercise we get the *solid contour curves* superimposed in the same plot. Of course, we are no longer showing the color gradient as done in the transverse mass case. The transformation of the dashed contour lines into corresponding solid ones (the same color represents the same value of that contours) within the same region qualitatively indicates the effect of this additional mass constraint. Minimum of these solid contours represents M_{2Cons}, displayed by circled plus $\oplus$ in the same figure. Note that the longitudinal momenta components for the invisible pairs are eliminated in this demonstration by minimizing with the G mass-shell constraint.

As noted, the m_G constraint restricts the invisible momenta making the region shrink as depicted by the dashed and solid contours (*e.g.* blue lines correspond to 100 GeV). The dashed line contour does not satisfy the additional G mass-shell constraint while the solid contour does. The same is true for all other lines as well. The representative values of M_{T2} and M_{2Cons} considered in this example are 75.1 and 98.5 GeV, respectively, for trial mass $\tilde{m}_\chi$ at 10 GeV which is smaller than the true invisible mass 100 GeV. The corresponding true mass of parents and heavy resonance are 200.0 and 1000.0 GeV, respectively. The white dashed

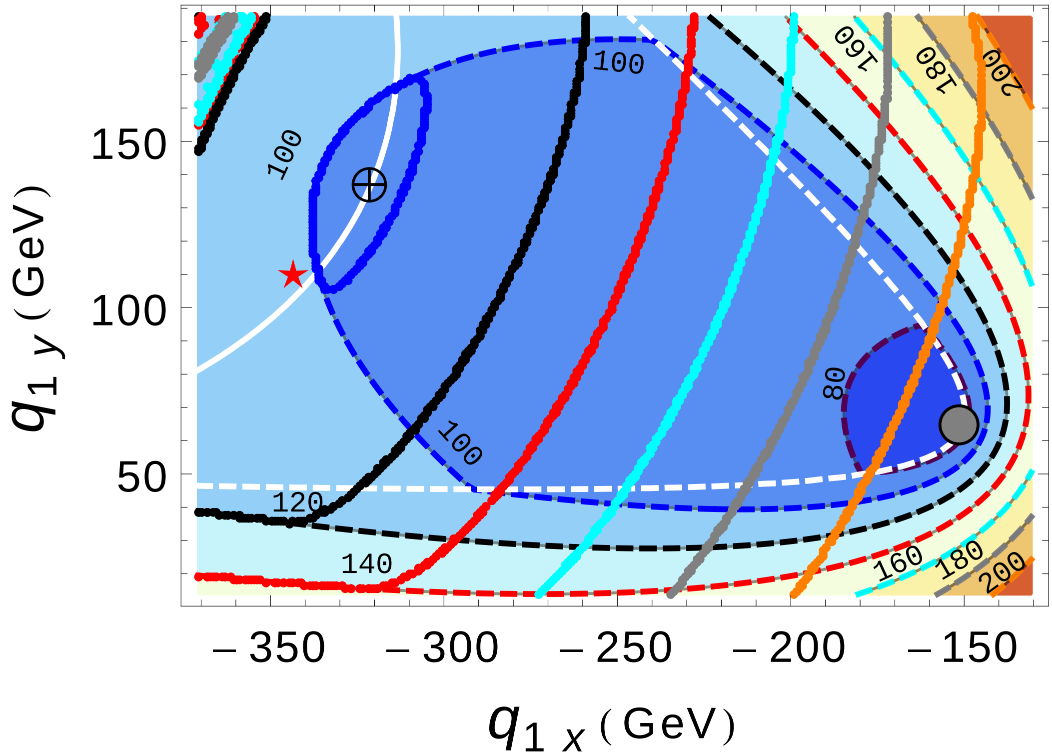

Figure 3.4: The effect of the heavy resonance mass-shell constraint is demonstrated using the mass variables M_{T2} and M_{2Cons} considering one antler event in the invisible momentum component space. The region represented by the color gradient is the maximum among two transverse masses coming from two decay chains. Corresponding contours are shown with dashed lines. Following eq. 3.1, the minimization of this quantity, M_{T2}, is represented by the filled circle ●. In the same plot, the solid lines (of the same colors) are delineating the corresponding contours for the $(1+3)$-dimensional new variable with heavy resonance mass-shell constraint as in eq. 3.24. Note that only the contour lines are shown in this case, not the color gradient as in the transverse mass case. The minimum of these solid contours is represented by the M_{2Cons}, displayed by circled plus $\oplus$ in the same figure. The G mass-shell constraint restricts the invisible momenta, making the region shrink, as depicted by the dashed and solid lines. The white dashed (solid) line represents the equality of transverse-mass (mass) of parents and this equality line is also moving towards higher values because of the constraint. The red star ★ is the position of true transverse momenta of invisible particle. The mass spectrum we choose is $(m_G, m_P, m_\chi) = (1000.0, 200.0, 100.0)$ in GeV and the trial invisible particle mass $\tilde{m}_\chi$ we took for this plot is 10.0 GeV.

(solid) line represents the equality of the transverse-mass (mass) of the parents and this equality line has moved towards higher value because of the constraint. As a result, one naturally expects $M_{2Cons} \geq M_2$ event by event. The red star ★ is the position of the true transverse momenta of the invisible particle. Clearly,

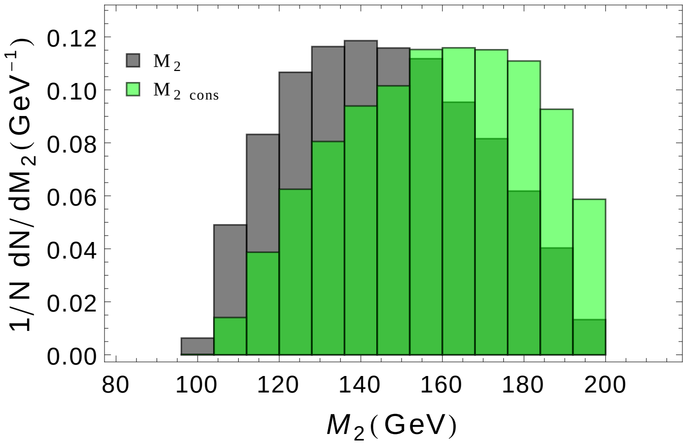

Figure 3.5: Normalized distributions of the mass variables are delineated using a toy model of antler topology with parents mass at 200 GeV. Both the M_2 (black) and M_{2cons} (green) distributions, considering the invisible particle mass at its true value (100 GeV), produce the end point at the correct parent mass. However, the heavy resonance constraint gives M_{2cons} a higher value, resulting a larger number of events at the end point.

the constraint brings the minimum, M_{2Cons}, closer to the true momenta, and this can improve any effort to reconstruct the invisible momenta. This feature will be further considered and discussed in Sec. 3.5.

One more remarkable feature which emerges at this point is the appearance of a kink which will be capitalized on in the next section. We already noted the event wise upward shift of values under the constraint. The next natural question in this context concerns the maximum value achievable by this mass variable and how it is related to the trial missing particle mass. The experimentally measured maximum can deviate (downward) from the theoretical maximum of the mass variable depending upon the accessible number of events, and more importantly, the abundance of events towards the end point of the distribution. We postpone this issue for the time being and consider it again in Sec. 3.4. Now coming back to our variable, it should not be surprising that at the true value of the invisible particle mass (*i.e.,* when $\tilde{m}_\chi = m_\chi$), the maximum value of the constraint variable M_{2Cons}^{max} coincides with that of the variable without this constraint, M_2^{max}. This is because both of these variables are derived for the same topology. On the other hand, for all other trial mass values, not only is the individual (event-by-event) constraint quantity larger, but also the maximum of that constraint mass is the larger value. To write in a compact form,

$$M_{2Cons}^{max}(\tilde{m}_\chi) \begin{cases} = M_2^{max}(\tilde{m}_\chi) = m_P, & \text{if } \tilde{m}_\chi = m_\chi \\ > M_2^{max}(\tilde{m}_\chi), & \text{if } \tilde{m}_\chi \neq m_\chi. \end{cases} \tag{3.25}$$

While this point is further discussed in the following section as a means of measuring the unknown masses, here we illustrate it with one example distribution for the aforementioned M_2 variables, considering a toy process with an antler topology as shown in fig. 2.1. For demonstration purposes, we choose a mass spectrum with $\{m_G, m_P, m_\chi\} = \{1000, 200, 100\}$ in GeV, which is a relatively difficult region for the kinematic cusp method [84, 85] known as the "large mass gap" region, where the cusp may not be very sharp, leading to large errors in the mass determination. The M_{2Cons} variable can be effective for mass determination both in the large mass gap region as well as in other regions of phase space. In fig. 3.5, we have compared the normalized distributions for M_2 and M_{2Cons} at the true mass of the invisible particle. Both the constrained (green histogram) and unconstrained (dark histogram) distributions share the same end point precisely at the parent mass, as argued earlier. However, from the distribution, one should also note the movement of the events towards the higher value under the heavy resonance constraint and, thus, expect a larger number of events at the end point.

3.3 Mass measurements with kink

In the last section, we defined the constrained variable M_{2Cons} using the heavy resonance on-shell constraint in the minimization of M_2. Analogous to the previous discussion,[4] the maximum of this variable M_{2Cons}^{max} also exhibits different dependencies on either side of the true mass, as a function of the trial invisible particle mass $\tilde{m}_\chi$. Following the eq. 3.25, one can obtain the kink structure ex-

[4]At this point, we would like to make it clear that the effect of ISR/UTM is not considered in this present analysis. This study shows a new kink solution due to the kinematic constraint coming from on-shell mass resonance in antler events. If one considers such events associated with ISR, that may marginally contribute to strengthening the already strong kink solution as demonstrated.

actly at the true mass. However, the reason for the appearance of this kink is attributed to the heavy resonance mass-shell constraint in the minimization.[5] Although there is no analytic formula in support of the above empirical observation, we verified it by checking the slope numerically before and after the true mass point. The presence of this kink is also authenticated by various mass spectra. Also, note that unlike $M_2^{max}(\tilde{m}_\chi)$, the constrained variable $M_{2Cons}^{max}(\tilde{m}_\chi)$ cannot increase forever with the increase of the trial invisible particle mass $\tilde{m}_\chi$, owing to the additional heavy resonance mass-shell constraint. M_{2Cons}^{max} can maximally reach up to half of the resonant mass and after that it would be unphysical. We have not studied the effects of ISR or UTM on this kink solution leaving these realistic studies for future work, but one expects that the presence of those extra transverse momenta will sharpen the kink structure.

To demonstrate this behavior in a more quantitative sense, we once again consider the toy process with the antler topology with the aforementioned mass spectrum. The top panel of fig. 3.6 depicts the dependence of both $M_2^{max}(\tilde{m}_\chi)$ and the constrained $M_{2Cons}^{max}(\tilde{m}_\chi)$ on the trial invisible particle mass $\tilde{m}_\chi$. The red thin dotted lines showing true mass lines intersect at the true mass point, $\{m_\chi, m_P\} = \{100, 200\}$ in GeV. This plot clearly illustrates that because of the on-shell constraint, M_{2Cons} attains a larger value, even bigger than the corresponding M_2^{max} once $\tilde{m}_\chi$ is different from the true mass m_χ. However, both of these maximum quantities attain the same value precisely at the true mass. The most compelling observation about this plot is the appearance of a kink exactly at this point for $M_{2Cons}^{max}(\tilde{m}_\chi)$, which can be used for measuring both masses m_P and m_χ simultaneously. The bottom plot describes the variation of difference between two maxima *i.e.*, $M_{2Cons}^{max}(\tilde{m}_\chi) - M_2^{max}(\tilde{m}_\chi)$ with respect to the trial invisible particle mass $\tilde{m}_\chi$. As expected, this difference between both the end points should ideally be zero at the true invisible particle mass.

[5] One can argue that the heavy resonance constraint works in the same spirit of 'relative' constraint as defined in M_2 class of variables [70]. In fact, in a non-antler scenario the M_2 variables under usual relative constraints extend/shift their distribution end-point value over and above the end point where this relative constraint is absent. Similar to our case, this can happen when the trial mass deviates from the true invisible particle mass. Hence, one expects formation or consolidation of a similar kink structure.

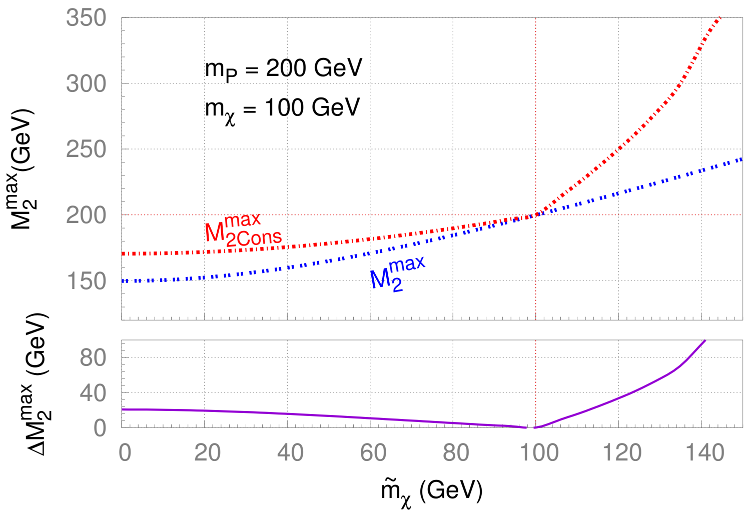

Figure 3.6: The upper panel depicts the behavior of the upper end points for both constrained $M_{2Cons}^{max}(\tilde{m}_\chi)$ and unconstrained $M_2^{max}(\tilde{m}_\chi)$ variables with respect to the trial invisible particle mass $\tilde{m}_\chi$. The blue dashed line portrays $M_2^{max}(\tilde{m}_\chi)$, the red dashed line $M_{2Cons}^{max}(\tilde{m}_\chi)$ and the red thin dotted lines intersect at the value of true masses. This plot clearly illustrates that because of the on-shell constraint, M_{2Cons} attains a larger value, even bigger than the corresponding M_2^{max} once $\tilde{m}_\chi$ is different from the true mass m_χ. The most compelling observation about this plot is the appearance of a kink exactly at the true mass point for $M_{2Cons}^{max}(m_\chi)$, which can be used solely for measuring both m_P and m_χ simultaneously. The lower panel describes the difference $M_{2Cons}^{max}(\tilde{m}_\chi) - M_2^{max}(\tilde{m}_\chi)$ with respect to the trial invisible particle mass $\tilde{m}_\chi$. As expected, the difference between both the end points is zero at the true invisible particle mass.

3.4 More aspects of kink measurement

One of the significant challenges with most of the mass variables is the detection of the distribution end point, which can reach the theoretical maximum only after using a large amount of data. The problem comes from the fact that a negligible amount of events typically contributes towards the distribution end point. M_{2Cons} is also not an exception, forming a tail in the distribution towards its maximum value.[6]

This feature is clarified in fig. 3.7 where the density of events is displayed as a percentage of the total data contributing to the M_2 distribution. As a function of the trial invisible mass $\tilde{m}_\chi$, the left plot shows the reference density for the M_2

[6]On the contrary, at the true invisible mass, M_{2Cons} produces a sharper end point as demonstrated in fig. 3.5.

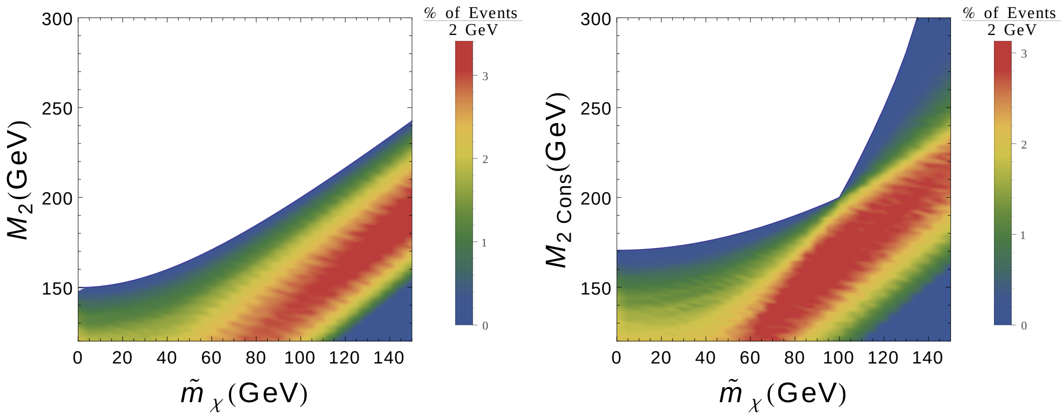

Figure 3.7: Density of events as a percentage of total data contributing to M_2 distributions as a function of the trial invisible mass $\tilde{m}_\chi$. On the left, the reference figure is shown for the M_2 variable which does not include heavy resonance constraint. The similar figure on the right is for the constrained variable M_{2Cons}, where constraint refers to the G mass-shell constraint. The color coding represents the percentage of events per 2 GeV bin in M_2. Since this distribution reaches a maximum for every trial value of $\tilde{m}_\chi$, above which there are no events, this disallowed range is kept as white. This upper end point in each plot represents the maximum curve shown in fig. 3.6. The presence of the kink can be clearly seen from the figure, and it is solely because of the on-shell heavy resonance constraint. But the reconstruction of the kink can be challenging due to the much smaller number of events at the endpoint, specifically when away from the kink. Also, it is interesting to note the changes in the event density due to the application of an additional constraint. Evidently, a significant number of events shifted towards the end point at the true mass, as can be observed in the figure.

distribution which can reach up to a maximum, above which there are no events and it remains white. For the same data set, the right panel shows the density of events for the constrained variable M_{2Cons}. The color coding represents the percentage of events per 2 GeV bin in M_2. These upper end points are equivalent to the maximum curve in fig. 3.6, in the last section. Compared to the left figure, M_{2Cons} developed a clear kink solely because of the on-shell constraint of the heavy resonance. One notices that a tiny fraction of events actually contributes at the end point, specifically when away from the kink position. Also, it is interesting to note the changes in the event density due to the additional constraint. At the true mass (kink), a significant number of events shifted towards

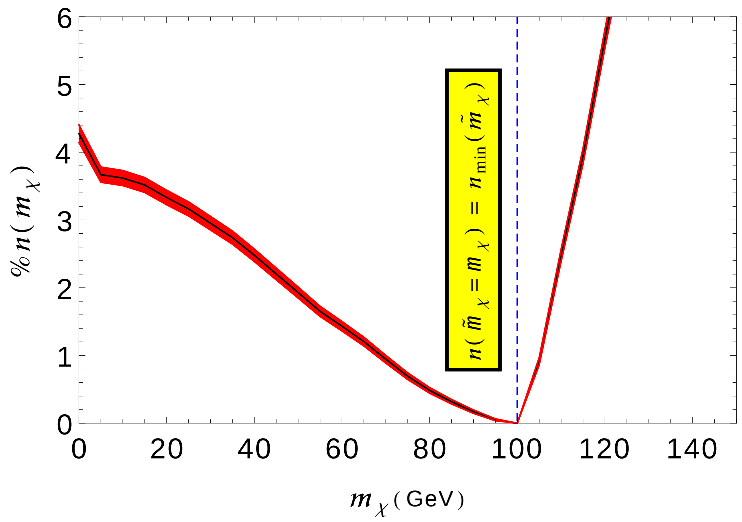

Figure 3.8: The variable $n(\tilde{m}_\chi)$ is shown with the black line and the blue line corresponds to the position at which the function exhibits its minimum. This minimum is exactly at the true value of the invisible particle. The effectiveness of the variable $n(\tilde{m}_\chi)$ as defined in eq. 3.26 is in identifying the minimum and thus measuring the true mass of the invisible daughter. The function as a percentage of the event fraction clearly shows a sharp minimum at $\tilde{m}_\chi = m_\chi$. So by identifying the minimum of $n(\tilde{m}_\chi)$, one can measure the invisible particle mass accurately. The red band shows the error accounting only for the statistical uncertainty.

the end point, as is also observed in fig. 3.5. This demonstration is also generated considering a toy process with an antler topology with the aforementioned mass spectrum $\{m_G, m_P, m_\chi\} = \{1000, 200, 100\}$ in GeV.

We pointed out and discussed the difficulty in determining the end points, which is in no way a shortcoming for this variable only. Fortunately, in this present case, the ability to simultaneously identify both M_2 and M_{2Cons} provides a solution for effectively pointing out the kink using all the events, not just relying on the events at the maximum.

We have already discussed in Sec. 3.2 that the additional constraint pushes the M_{2Cons} towards the higher value compared to M_2, such that, as long as the trial invisible mass $\tilde{m}_\chi$ is unequal to the true mass m_χ, there can be enough events generating a larger M_{2Cons} than M_2^{max}. Moreover, it is clear from eq. 3.25 that the M_{2Cons}^{max} coincides with M_2^{max} at the true invisible mass. This enables us to define a dimensionless variable pointing out the position of the kink, in a way that was originally proposed in [61]. For a given $\tilde{m}_\chi$, one counts all the events having M_{2Cons} value larger than the corresponding M_2^{max} to get the fraction,

$$n(\tilde{m}_\chi) = \frac{1}{N}\mathcal{N}(\tilde{m}_\chi) = \frac{1}{N}\sum_{i=1}^{N}\mathcal{H}((M_{2Cons}(\tilde{m}_\chi) - M_2^{max}(\tilde{m}_\chi))_i). \tag{3.26}$$

Here, i is the event index with total number N. $\mathcal{N}(\tilde{m}_\chi)$ is the number of events in which $M_{2Cons}(\tilde{m}_\chi) > M_2^{max}(\tilde{m}_\chi)$ for any given $\tilde{m}_\chi$, satisfied by the Heaviside step function,

$$\mathcal{H}(y) = \begin{cases} 0, & \text{if} \quad y \leq 0, \\ 1, & \text{if} \quad y > 0. \end{cases} \tag{3.27}$$

It is easy to follow from eq. 3.25 that the quantity $n(\tilde{m}_\chi)$ should ideally be zero at the true mass m_χ, since both M_{2Cons} and M_2 share the same maximum value at that point. However, on both sides away from this point, substantial events contribute above the M_2^{max}; hence, $n(\tilde{m}_\chi)$ poses a sharp minimum at the true mass point. If other realistic effects, such as backgrounds, mass width, and experimental errors are considered there would be some finite number of events present at the minimum rather than zero. These effects are not considered in the present analysis. However, it is safe to assume that the position of the functional minimum can be correctly identified to get the true invisible mass. The advantage of using $n(\tilde{m}_\chi)$ is that it does not rely on some isolated event at the end point but rather it relies on a significant number of events distributed on a band in a two-dimensional plane between M_2^{max} and M_{2Cons}^{max} which contribute to establish this minimum.

In our example, the theoretical prediction of the function $n(\tilde{m}_\chi)$ (as a fraction of total events) is shown in fig. 3.8. The red band is the error accounting only for the statistical uncertainty. One can clearly identify the minimum and justify the relation,

$$n(\tilde{m}_\chi = m_\chi) \equiv n_{min}(\tilde{m}_\chi), \tag{3.28}$$

to measure the invisible particle mass accurately. Hence, it is straightforward to measure both the parent and daughter masses simultaneously.

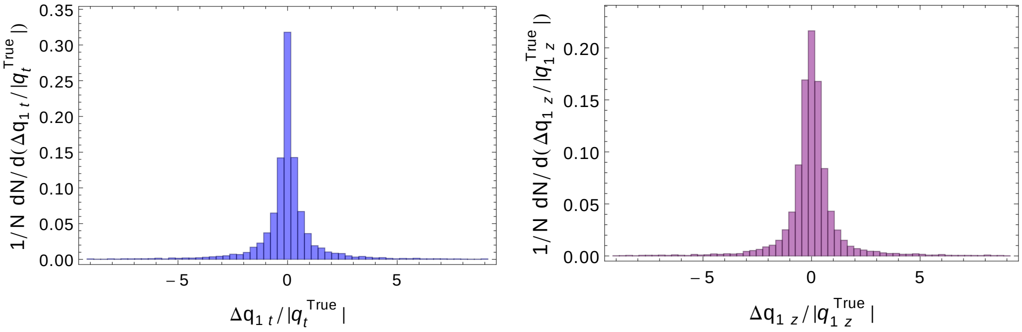

Figure 3.9: Capability of reconstructing missing daughters momenta is demonstrated using constrained variable. The left figure displays a normalized distribution of $\frac{\Delta q_{1t}}{|q_{1t}^{True}|}$ with $\Delta q_{1t} = q_{1t}^{reco} - q_{1t}^{True}$, hence parameterizing the deviation from true momenta for the transverse part, with "t" referring to either x or y-component of momenta. This reconstruction of momenta is done from the minimization of the M_{2Cons} with the true mass of the invisible particle as input. The reconstructed invisible momentum is unique and very well correlated with true momentum as the distribution of $\frac{\Delta q_{1t}}{|q_{1t}^{True}|}$ has a sharp peak at zero. In a process where the invisible particle mass is unknown, $n(m_\chi)$ can be used for invisible particle mass determination and then event reconstruction using M_{2Cons}. Similarly, the right figure displays a normalized distribution of $\frac{\Delta q_{1z}}{|q_{1z}^{True}|}$ with $\Delta q_{1z} = q_{1z}^{reco} - q_{1z}^{True}$ for more troublesome longitudinal momentum. Once again, q_{1z} reconstruction is unique and well correlated with true longitudinal momenta of invisible particle.

3.5 Reconstruction capability of events

In this section, we want to explore the event reconstruction capability coming from the constrained mass variable M_{2Cons}, typically once the invisible particle mass is determined, as in last the section. Event reconstruction is extremely important in the case of spin, polarization and coupling determination of new physics particles as well as of the Higgs boson and the top quark in SM processes. However, it is almost impossible to determine them exactly for a scenario involving multiple invisible particles in a hadron collider, especially for a topology with a short decay chain. Attempts have been made to reconstruct events using the transverse mass variable M_{T2} [81, 82, 86] known as the M_{T2}-assisted on-shell (MAOS) method in which the transverse momenta of the invisible particles are determined from the minimization of M_{T2}, and the longitudinal components are determined by solving the mass-shell constraints of parent and daughter. In refs. [87, 88], it is shown that $\hat{s}_{min}$ and its constrained sisters $\hat{s}^{cons}_{min}$ and $\hat{s}^{cons}_{max}$, can also be used for event reconstruction especially in antler topology, where constraints refer to missing transverse momenta and available mass-shell constraints in an event. The reconstructed momenta of the invisible particles are derived at the extremum of $\hat{s}$ and the constrained $\hat{s}$ variables.

In this section we reconstruct all components of the invisible particle momenta from minimization of the $(1+3)$-dimensional variable M_{2Cons} with the true mass of the invisible particle as input. The capability of reconstructing the missing daughter momenta is demonstrated in fig. 3.9 using this constrained variable. The left plot displays a normalized distribution of the fractional deviation (or error) in this reconstructed quantity from that of the true value, in the case of transverse part of the invisible momenta. This deviation is parametrized using a ratio defined as

$$\frac{q^{reco}_{1t} - q^{True}_{1t}}{|q^{True}_{1t}|}, \tag{3.29}$$

where the subscript "t" refers to the transverse (x or y) component of the momenta. The reconstructed invisible momenta are proved to be unique and very well correlated with the true momenta, as the observed distribution has a sharp peak at its true value (*i.e.,* zero deviation). Similarly, the right figure displays a normalized distribution of the corresponding variable for longitudinal momentum, and once again one gets a unique reconstruction well correlated with the true longitudinal momenta of the invisible particle. In a process where the invisible particle mass is unknown, $n(m_\chi)$ can be used for invisible particle mass determination, and then events can be reconstructed using M_{2Cons}.

Chapter 4

Reconstructing semi-invisible events from Higgs

In this chapter we will discuss the reconstruction of semi-invisible tau-lepton pair events using the constrained mass variable M_{2Cons}. Before reconstructing the tau pair events we will discuss the motivation for studying tau-lepton and some earlier methods which will subsequently be compared to our method.

The Large Hadron Collider (LHC), still lacking in its objective of confirming any clear indication of new physics beyond the Standard Model (SM), has nevertheless successfully discovered the SM like Higgs boson at 125 GeV [3, 4] and also made tremendous progress in probing different properties of this newly discovered scalar [89, 90]. Owing to the relatively large Yukawa coupling, looking for events where the Higgs decays into third generation τ's is the natural first step in exploring interactions with leptonic modes. Full event reconstruction for such an event topology is especially important, since fermions from the third generation hold the key to electro-weak symmetry breaking, and moreover, can shed light on different aspects of the resonant state such as, coupling structure, spin and CP properties. This, in turn, can be exploited to constrain effects coming from any possible new physics.

The CMS collaboration recently studied [91] tau pair production from the Higgs boson, at center-of-mass energies 7 and 8 TeV, corresponding to integrated luminosities of 4.9 and 19.7 fb^{-1}, respectively. To explore these τ leptons, both hadronic and leptonic decay modes are considered, resulting in six different final states from the pair. This analysis reported an excess of events over the background only hypothesis, with a local significance 3.2 standard deviations corresponding to the Higgs boson mass at 125 GeV. The study of τ pair final state at the LHC is rather onerous, making the significance of signal smaller compared to other decay modes of the Higgs boson. The difficulty lies in reconstructing the hadronic or leptonic decay modes of the tau lepton, especially in the presence of invisible neutrinos in the final state.

There are several techniques introduced for the study of the $h \to \tau\tau$ process and we give an outline as follows.

- ◇ *Collinear approximation* [92] assumes that all the decay products from the tau lepton are collinear. As a result, each neutrino, among these decay products, takes some fraction of the tau momenta. This unknown fraction can be determined by using the measured momenta of the visible particles and missing transverse momentum. This approximation is effective when the Higgs is produced in association with hard jet(s), boosting the tau pair system. Thus, a significant portion of events, producing the τ's back-to-back in transverse direction, remains outside the purview of this method. Therefore, the overall statistical significance from such study gets reduced.

- ◇ *Missing mass calculator* [93] replaces the collinear approximation by constructing a probability function utilizing the angular information in the event to parameterize this under-constrained system. Two remaining unsolved degrees of freedom are thus fixed, whereas, the rest are solved using the four constraints with τ mass-shell relations, and the missing transverse momenta. Missing mass calculator is applicable to all events, although it is computationally expensive.[1]

- ◇ *Displaced vertex method* [95] considers the events in which at least one of

[1] Recently, a method [94] similar to the missing mass calculator, is proposed. This study samples all kinematically allowed values of the magnitude of invisible momentum and the visible/invisible invariant mass using their distributions from the Monte Carlo simulations. The mass of the heavy resonance is shown to be the position of maximum probability.

the τ's undergoes a three-prong decay. This method reconstructs the τ momenta using the secondary vertex information, together with the mass-shell and missing transverse momentum constraints. This method can utilize only a small fraction of events associated with 3-prong decay of tau.

◇ *Constrained $\hat{s}$ method* [87, 88] assumes the knowledge of the parent mass (m_τ in present process) and minimizes the partonic Mandelstam variable with respect to the unknown invisible particle momenta, taking care of missing transverse momentum constraints, to construct $\hat{s}^{cons}_{min}$ and $\hat{s}^{cons}_{max}$ variables. The new variable $\hat{s}^{cons}_{min}$ ($\hat{s}^{cons}_{max}$) exhibits a sharp endpoint (threshold) exactly at the Higgs mass.

◇ *Stochastic mass-reconstruction* [96] is another prescription proposed lately for the measurement of the mass of a heavy resonance decaying into tau pair. This method estimates the momentum of the parent particle (τ) by multiplying the final state daughter multiplicity with the average momenta of visible daughters.

Before discussing the new reconstruction method, we start with investigating yet another method based on the MAOS technique. We reconstruct the invisible momenta, followed by calculating the τ pair invariant mass. One expects a correct reconstruction of the heavy resonant mass if the true invisible momenta were already available. In the absence of that information, the efficiency of any such reconstruction technique, in calculating the event momenta, is best represented by demonstrating the derived invariant mass. The benefit of this MAOS method is in its applicability for all events and in a simple M_{T2} based calculation for this topology with two semi-invisible tau decay chains. More importantly, it motivates one to use the (1+3) dimensional sister M_{2Cons}, which preserves all the properties of M_{T2}. In addition, this new variable has the ability to utilize the on-shell mass information including that of the Higgs and thus improves the reconstructed momentum and mass for this semi-invisible system. Already measured Higgs mass information at the LHC is utilized in the construction of the proposed variable M_{2Cons}, significantly improving the event reconstruction capability over the existing methods. Although, in the present study we focus on the reconstruction of the SM Higgs boson decaying into the tau lepton pair events, this technique is in general applicable for the reconstruction of any heavy resonance producing a pair of unstable particles, which subsequently decay semi-invisibly. This is typically antler [84] type production mechanism which can be mediated either by a light or heavy scalar, or heavy Z' like vector boson, or some spin-2 resonance. Once the mass of the heavy resonance is known, the M_{2Cons} can be used for a better event reconstruction and thus looking into different properties of this heavy particle.

The rest of our presentation is organized as follows. In section 4.1, we give a short outline of the collinear approximation describing the principle to calculate invisible momenta before moving to our scenario. We introduce the M_{T2} assisted method, MAOS, and once again reconstruct the events using this technique. We compare the reconstruction efficiency in both cases by constructing the τ pair invariant mass. Knowing the mass of the Higgs boson already, we thereafter introduce the (1+3) dimensional generalization M_{2Cons} which, by exploiting this constraint, is expected to give an improved measurement over M_{T2}. Event reconstruction efficiency for longitudinal and transverse momentum components are discussed in section 4.2 and comparison is made between these methods.

4.1 Existing reconstruction methods for $h \to \tau\tau$ events

The collinear approximation is one of the most popular methods used for the reconstruction of the invariant mass $m_{\tau\tau}$ in semi-invisible decay of the $h \to \tau\tau$ process. The primary assumptions associated with this method are that all decay products of the τ lepton are collinear and the source of missing transverse momenta is the neutrinos only. Following the above mentioned presuppositions, the visible decay products from each τ take some fraction of the respective τ momentum, f_i with $i = 1, 2$. So in a particular event these two unknown fractions can be solved using missing transverse momentum constraints. As a result, full

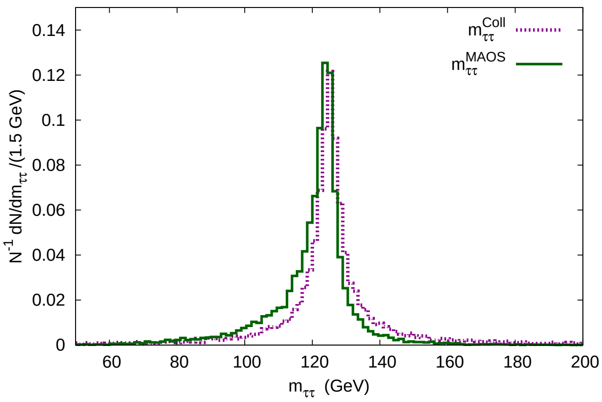

Figure 4.1: The purple-dotted histogram delineates the normalized distribution of τ pair invariant mass $m_{\tau\tau}$, calculated using the collinear approximation. Similarly, in the same plot, the green-solid histogram describe the same quantity utilizing the MAOS momentum reconstruction method. The peak position of both these distributions are at the Higgs mass implying comparable efficiency.

reconstruction of the event is possible. But when the Higgs boson is produced with small (zero) transverse momentum the two τ leptons are going back-to-back in the transverse direction, making the reconstruction of τ momenta impossible. The situation can be surpassed if the Higgs boson is produced with sufficient non-zero transverse momentum, that may come from associated production of initial state radiation (ISR) or extra hard jet(s).

The full reconstruction of these semi-invisible tau-lepton pair events requires the reconstruction of the neutrino momenta. The neutrino momentum in terms of visible particle momenta is $\vec{q}_i = \vec{p}_{\tau_i} - \vec{p}_i = F_i \vec{p}_i$, where $F_i = \frac{1}{f_i} - 1$, and p_{τ_i} are momenta of τ's in the $h \to \tau\tau$ process, while p_i and q_i are the final visible momenta and neutrino momenta respectively from each of these τ_i decay. We are following this momentum convention throughout this chapter. The two unknown fractions f_i can be solved using the following two transverse equations

$$\vec{\not{p}}_T = \sum_i F_i \vec{p}_{iT}. \tag{4.1}$$

The solutions for f_i are,

$$f_1 = \frac{1}{1+r_2}, \;\; f_2 = \frac{1}{1+r_1}, \tag{4.2}$$

with $r_i = \left|\frac{\not{p}_y p_i^x - \not{p}_x p_i^y}{p_1^y p_2^x - p_1^x p_2^y}\right|$ positive dimensionless ratios constructed in terms of measured momentum combinations. The invariant mass of the $\tau\tau$ system using the collinear approximation is $\frac{m_{vis}}{\sqrt{f_1 f_2}}$, where m_{vis} is the total invariant mass of all the visible particles. In fig. 4.1, we have presented the normalized distribution for the invariant mass $m_{\tau\tau}$ (in purple-dotted histogram), calculated using the collinear approximation. The peak of the distribution is exactly at the Higgs mass.

Now it is evident from the eq. 4.2 that when the two τ's are back-to-back in the transverse direction the collinear approximation fails to work. Similar arguments can be realized in terms of azimuthal angle [93]. Here, parton level simulated events[2] for $h \to \tau\tau$ are generated along with the ISR jet(s) using PYTHIA 8 [97] and thereby making a suitable momentum configuration for the collinear approximation to work. One can also notice from the histogram that the collinear approximation shifts the reconstructed invariant mass towards a higher value, and also develops a tail at larger invariant mass. This is a consequence of some of the events coming with soft (ISR) jets. This tail becomes rather significant once realistic events with measurement errors are also included [93]. Subsequently, the information of the heavy resonance mass is utilized in addition to the collinear approximation for the full reconstruction of the tau pair events [98]. This additional constraint improves the reconstruction of tau lepton momenta. This technique is effective even if the tau leptons are produced nearly back-to-back in transverse plane as happens for a significant portion of events. In the present analysis we have already considered the Higgs boson produced with sufficient transverse momenta balanced by ISR jet(s). So this tail feature in the distribution (as noted in fig. 4.1) is not prominent and this provides an estimate

[2]Note that the default setting in PYTHIA 8 generates both the hadronic and leptonic decay of tau preserving spin correlations based on fully modeled τ lepton decay. Along with that, in our present analysis, we generate parton-level simulated events keeping the hadronization option off, leaving the realistic analysis including the particle identification and detector level simulation for future work.

of the efficiency which one expects after using the resonant mass constraint.

We now move to examining the ability of MAOS [81, 82], a M_{T2}-based (M_{T2} assisted on-shell) method, for the full reconstruction of the tau pair events. M_{T2} [49, 53] is defined as the maximum of transverse mass, constructed for each τ using missing transverse momentum constraints, minimized over the invisible particle momenta. In the MAOS method transverse momenta of the invisible particles are assigned to the values that give this minimization. The longitudinal momentum is further determined using the two mass-shell conditions $(p_i + q_i)^2 = m_{\tau_i}^2$. Hence, the MAOS method reconstructs the full event with a four fold ambiguity, arising because of the quadratic mass-shell constraints.

The mass of the heavy resonance can be constrained by calculating the invariant mass of both the τ's, $m_{\tau\tau}^{MAOS}$, with their assigned MAOS momenta, $p_{\tau_i}^{MAOS}$, where $p_{\tau_i}^{MAOS} = p_i + q_i^{MAOS}$ and the full four fold ambiguity is taken into account by the superscript $MAOS$. In the same fig. 4.1, we have also shown the normalized distribution (green-solid curve) considering this MAOS reconstruction and recognize that both the methods display equal level of efficiency in reconstructing the invariant mass. Note that we utilize the same Higgs data associated with an additional jet[3] for this analysis. That was essential for the collinear approximation to work, but the MAOS method can be applied to all momentum configurations of the considered process, leading to a statistical advantage over the collinear approximation. The same argument is also true for our proposed method which we would discuss next.

We now explore whether the event reconstruction can be improved using MAOS along with the heavy resonance mass shell constraint. Since MAOS assigns the transverse momenta from the minimization of M_{T2}, a (1+2) dimensional variable, q_T^{MAOS} can not be constrained by the heavy resonance mass. But MAOS uses (1+3) dimensional mass shell constraints to assign longitudinal momentum. So the heavy resonance mass shell constraint may be used along with parent mass to get longitudinal momentum. But the full event reconstruction may not

[3]Therefore we actually used the subsystem based M_{T2}^{sub}[58] but to avoid cumbersome notation we simply write it as M_{T2} (also similarly in case of M_2) in this whole chapter.

be improved. We now look at the possibility to construct the mass variable where this mass constraint can be used more inclusively.

We shift our focus from transverse mass variables to M_2, which is a (1+3)-dimensional variable [19, 70, 80] used for the determination of mass of the unstable particle, produced in pair and decaying semi-invisibly. This variable can use the longitudinal momentum component information which enables it to use available mass-shell constraints of resonance particle. This capability was lacking in its predecessor M_{T2}, although, this is an efficient variable for mass and spin measurement. As discussed in chapter 3, after executing the additional minimization over the z-components of invisible particle momenta, M_2 comes out to be exactly equal to its (1+2)-dimensional analog, M_{T2} [70]. Hence, all the properties of M_{T2} transmit to its successor M_2 with additional advantages, accommodating the on-shell mass constraints as discussed earlier. One important property of the M_2 (or M_{T2}) is that, by construction, this quantity needs to be less than or equal to the unstable parent mass, m_τ, given a massless invisible daughter hypothesis ($\tilde{m}_\nu = 0$). So, over many events, the distribution of M_2 has an endpoint exactly at the true mass of the mother particle.

The distribution of M_2 mass variable considering the semi-invisible decay of tau pair is displayed in fig. 4.2 in green-dotted histogram. It is clear from the figure that the endpoint of M_2 is at m_τ, as expected. We have considered only the hadronic decays of τ's encompassing both the 1-prong and 3-prong decays. The tau lepton has a branching ratio of around 66% for hadronic decays of which 1-prong and 3-prong decay accounts for 50% and 15% respectively, while rest are other hadronic decays. Although the leptonic decay modes can have a considerable branching ratio together with a relatively better energy resolution, we have not considered these decay modes in the present analysis. With associated three to four neutrinos in the final state event reconstruction is impossible unless one invokes some kind of approximation.

Equipped with the Higgs mass (m_h), already measured in the first run of the LHC, M_2 can be further improved with this constraint and can prove to be useful in providing the invisible particle momenta with great efficiency. The

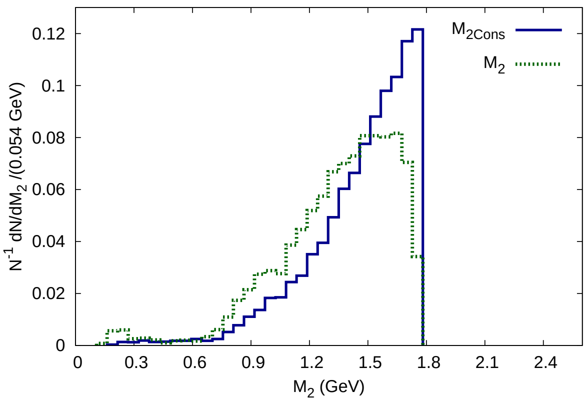

Figure 4.2: Normalized distributions for (1+3)-dimensional mass constraining variables in the process when Higgs decays semi-invisibly through τ pair production. Green-dotted histogram describes the M_2 distribution considering hadronic decays of τ, consisting of both 1-prong and 3-prong decays. As expected, the figure shows that the endpoint of this distribution is at m_τ mass. Similarly, the blue-solid histogram representing the M_{2Cons} also has endpoint at the same point. However, endpoint in this case is populated with much a larger number of events.

constrained variable was proposed in the chapter 3, in eq. 3.24.

The Higgs mass-shell condition further constrains the invisible momenta and thus making the allowed phase space shrink to a comparatively smaller region.[4] Hence, the derived value of M_{2Cons} comes out to be greater than or equal to M_2. Both of these quantities, considering each events, are bounded by the tau mass which satisfies the relation $M_2 \leq M_{2Cons} \leq m_\tau$. Consequently, more number of events move towards the endpoint in the distribution of M_{2Cons} in comparison to M_2. The distribution of M_{2Cons} is also shown in the fig. 4.2 in blue-solid curve which clearly demonstrates that the constrained variable M_{2Cons} exhibits a very sharp endpoint with large number of events present there, enabling a better mass measurement and momentum reconstruction which we discuss now.

[4]A detailed discussion on the squeezed phase space under the influence of additional mass-shell constraint can be followed from ref. [99].

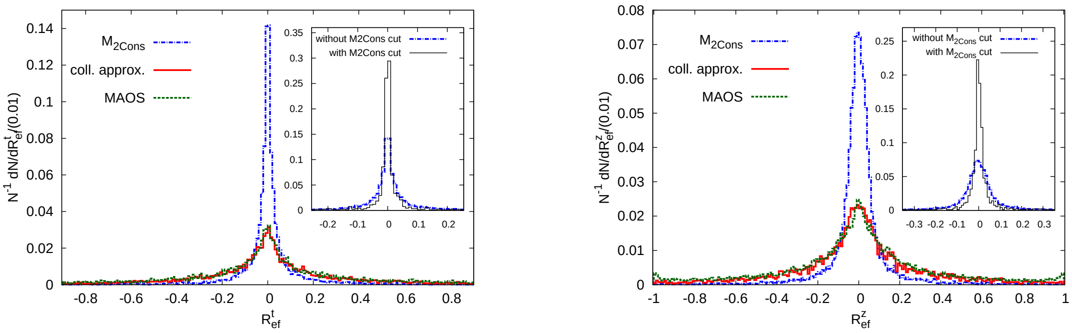

Figure 4.3: Efficiency of different methods for reconstructing events coming from semi-invisible Higgs boson decay through τ pair production, after considering hadronic decays of τ, consisting of both 1-prong and 3-prong decays. Deviation of the reconstructed momenta from the true invisible momenta are parameterized using two variables (left panel) R^t_{ef} for transverse part and (right panel) R^z_{ef} for longitudinal momentum. The distributions of these variables utilizing the M_{2Cons}, collinear approximation and MAOS method are exhibited in blue-dashed-dotted, red-solid and greed-dotted lines respectively. The event reconstruction capability of the collinear approximation and MAOS method are of same order (as seen in fig. 4.1) while M_{2Cons}, with the help of additional mass constraint, is showing significant improvement. (Inset plots) Efficiency of reconstruction for both the transverse part and longitudinal momentum comparing with and without using M_{2Cons} cut. We have selected 10% of events towards the upper endpoint of M_{2Cons} and the reconstructed momenta with these events are found to be highly correlated with the true momenta of the invisible particle in comparison to the full data set.

4.2 Correlation of reconstructed momenta with true neutrino momenta

In this section, we parametrize the efficiency of event reconstruction for $h \to \tau\tau$ using different methods including collinear approximation and argue the effectiveness in using the M_{2Cons} in calculating[5] the invisible particle momenta. Reconstruction of such events are of particular interest for spin, polarization, coupling

[5]We have calculated the mass variable M_2 and M_{2Cons} using constrained optimization method in Mathematica. Towards the end of this analysis, a generic package, OPTIMASS[24], for the calculation of mass variables appeared which is a Minuit2 based method. OPTIMASS can also be used for the calculation of M_{2Cons} with a simple modification of the constraint in the examples demonstrated there.

measurement and CP symmetry studies [100, 101]. We use two dimensionless parameters, R^t_{ef} for transverse (with t is either x or y component) and R^z_{ef} for longitudinal momenta, to determine the efficiency of event reconstruction.

$$R^t_{ef} = \frac{\Delta q_t}{|q_t^{True}|} = \frac{q_t^{Reco} - q_t^{True}}{|q_t^{True}|}, \tag{4.3}$$

$$R^z_{ef} = \frac{\Delta q_z}{|q_z^{True}|} = \frac{q_z^{Reco} - q_z^{True}}{|q_z^{True}|}. \tag{4.4}$$

By construction, the variables R^t_{ef} and R^z_{ef} acquire zero value once the reconstructed momentum matches with the true invisible particle momentum in a particular event. Hence, the efficiency of any reconstruction method is judged depending on the number of events having vanishing values of R^t_{ef} and R^z_{ef}. In other words, the sharper the peak of the distribution coupled with higher number of events, the better is the efficiency of reconstruction. It is straightforward to calculate R^t_{ef} and R^z_{ef} for collinear approximation, once the fractions f_i are known. In fig. 4.3, the left panel shows the distribution of R^t_{ef} utilizing the collinear approximation, MAOS and M_{2Cons} methods respectively. Similarly, the right plot displays the distribution of R^z_{ef} for all these methods. The reconstructed momenta using M_{2Cons} are shown to be unique and very well correlated with the true momenta of the invisible particle. It is evident from the figure that M_{2Cons} gives significant improvement in event reconstruction compared to the collinear approximation and MAOS method.

The efficiency of reconstruction for both the transverse part and longitudinal momentum from M_{2Cons} can be improved further by selecting events near the upper endpoint of M_{2Cons} distribution. Although, the additional constraint in M_{2Cons} already shifts its value towards the endpoint, an improvement over conventional MAOS calculation, one can still use a M_{2Cons} cut to improve the event reconstruction with higher statistics in comparison to MAOS as evident from fig. 4.2. In the inset plots of fig. 4.3, we compare the improvement in reconstruction efficiency using the M_{2Cons} selection. Only 10% of events are selected towards the upper endpoint of M_{2Cons} and the reconstructed momenta are proved to be highly correlated with the true momenta of the invisible particle in comparison with the full data set, at a price of event statistics.

Chapter 5

Summary and Conclusions

The Large Hadron Collider (LHC), after successfully completing its first run coupled with the remarkable achievement of the Higgs boson discovery, has already entered into its second phase. Upgraded with higher energy and luminosity, the main physics goal would be to explore the multi-TeV scale associated with physics beyond the Standard Model (BSM). Although LHC has not reported any clinching evidence for new physics so far, expectations are running high for possible new physics signals in the near feature unless such signatures are already hidden inside the LHC data. Any scenario with a positive outcome essentially demands the measurements of the mass, coupling and spin of new BSM particles. However, this is expected to be complex in many of the very likely scenarios with a wide class of BSM models which have incorporated the concept of thermal relic dark matter (DM) as some stable exotic member within them. These massive DM particles being colorless, electrically neutral and weakly interacting, once produced in the collider, does not leave any trace at the detector. Hence, one needs to rely on experimentally challenging signature of missing transverse momenta $\vec{\not{p}}_T$ from the imbalance of total transverse momentum, accounting for all visible products in each event from an already adverse jetty environment of the hadron collider. Moreover, DM in many models would be expected to be produced in pairs because of a stabilizing symmetry, commonly the Z_2 parity. As a result, common signatures, coming from such models at a high-energy collider, typically are detectable SM particles along with a pair of invisible particles. It is very strenuous to measure all the unknown masses or to fully reconstruct those events, with these kinds of signatures, at the large hadron collider.

In the light of dark matter models, missing energy signals would be looked for very carefully. The $\hat{s}_{min}$ variants of mass variables were designed for promptly finding the mass scale in a model independent way for any complex topology of BSM events associated with semi-invisible final state production. In the present analysis, we proposed to exploit additional partial information available in the event as constraints to improve the search. We classified our discussion based on two different classes of simple production topologies, widely available both in SM and BSM production, which are, antler and non-antler topologies.

The SM as well as new physics models predict antler production processes, including important Higgs production in the hadron collider. These topologies can be constrained significantly using additional intermediate mass-shell conditions. We have demonstrated, with different examples, that the constrained variable $\hat{s}_{min}^{cons}$ can significantly improve the distribution and the measurements. More interestingly, these additional constraints ensure a finite upper value of the $\hat{s}$ variable, defined as, $\hat{s}_{max}^{cons}$ which is not well-defined and finite in the unconstrained picture. Hence, this new variable can also be exploited to some extent. Apart from considering different BSM examples to demonstrate this variable in the context of sub-system topology and in the difficult signatures with more invisible final states in antler topology, we also demonstrated the effect of these additional constraints in a simple non-antler topology.

To clarify the effects of these constraints in the invisible momenta parameter space, we choose phenomenological examples explicitly demonstrating how these mass variables are restricted and pushed towards the true values of $\hat{s}$, together with their choice of the invisible momenta closer to the true ones. Hence, one can consider quantifying the capability of reconstructing the invisible momenta in present scenario. We have constructed and shown the efficiency of momentum reconstruction using these constrained $\hat{s}$ variables which predict a unique momentum associated with each of these mass-bound variables in each event.

Subsequently, we have studied the antler topology where intermediate and invisible masses are unknown unlike in the earlier case, but instead assume the knowledge of heavy resonance mass. There are several BSM scenarios, where the heavy resonance is produced before its semi-invisible decay into some visible decay products and other invisibles which are exotic dark matter particles. Our objective is to determine all the unknown masses, including those of the dark matter particles produced from the heavy resonance. We consider a new constrained variable M_{2Cons} extending the $(1+3)$-dimensional mass variable M_2, by implementing additional heavy grandparent mass-shell constraint in the minimization.

This new variable M_{2Cons} contains several interesting features. We demonstrate how this variable acquires an event-wise higher value owing to this constraint. In particular, we show how this variable moves closer to the unknown parent mass. In addition, the calculated invisible momenta at this minimum can provide a close estimate of the true momenta of the invisible particles for such events. Both these characteristic features are highlighted and exploited further to sharpen the measurements.

Another striking feature comes out once we analyze the distribution maxima of this new variable, $M_{2Cons}^{max}(\tilde{m}_\chi)$, as a function of the trial values of the unknown dark matter particle mass. This is constructed in an analogy with the popular study of $M_{T2}^{max}(\tilde{m}_\chi)$, which gives a useful correlation curve relating the parent mass with the invisible particle mass. But now, under mass-shell constraint, $M_{2Cons}^{max}(\tilde{m}_\chi)$ develops a new kink solution over the correlation curve exactly at the value where this trial mass coincides with the true mass. Hence, this opened another new avenue that produces a kink feature to measure both masses simultaneously.

To handle the sparseness of events towards the distribution end point, we analyze with an experimentally feasible observable $n(\tilde{m}_\chi)$ by utilizing both constrained and unconstrained variables. This observable does not rely on isolated events at the end point, but instead uses a significant amount of available data to pinpoint the unknown invisible particle mass from the sharp minimum.

Our method provides a complementary procedure to earlier antler studies and is applicable to any mass region. We demonstrated our analysis in the large mass gap region, considered as a difficult region for the kinematic cusp method. In this region, the cusps of many variables are not very sharp, which makes the mass determination more prone to error. But the M_{2Cons} method can be used safely for better accuracy. We also investigated the event reconstruction capability of M_{2Cons}, and we reconstruct the unknown invisible particle momenta at the constrained minimum. The reconstructed momenta are found to be unique and well correlated with the true invisible momenta.

We thereafter presented a detailed analysis by applying M_{2Cons} in reconstructing the semi-invisible tau-lepton pair produced from the Higgs boson . With increasing Higgs data, it is an exciting time to verify and validate different properties of the Higgs including the exploration of minuscule couplings in the leptonic sector. Along with the popular machinery using collinear approximation, we also looked into the efficiency of the MAOS method. We further examined the effectiveness of another variable in the M_2 class accommodating the Higgs mass information in the analysis. The variable, M_{2Cons}, is capable of providing a very accurate and unique reconstruction of such events.

We have studied the usefulness of the constrained mass bound variables for semi-invisible events produced at the LHC. The constrained $\hat{s}$ mass variables are associated with a sharp endpoint feature which can be helpful in pointing out the endpoint over the background events. Although consideration of backgrounds, width effect, detector resolution and other realistic effects will change the endpoint structure, the endpoint may still be identified. In addition, these variables provide a well approximated momentum to the invisible particles. The variable M_{2Cons} has many interesting properties *e.g.*, sharp endpoint, strong kink etc. which will help in quantifying all the unknown masses associated with a short decay chain simultaneously. These properties, even after including realistic effects, may be measured with improved statistics compared to earlier methods. Moreover, these constrained variables can be useful in distinguishing signal from background events, not just limiting our objectives in mass and momentum measurement. We, are therefore looking forward to appending these observables in the LHC toolkit for future analysis.

Once the masses and the invisible particle four momenta are determined, the next major task is to measure the spin, couplings etc. related to the new particles. In the future we would like to utilize these constrained mass variables for the spin and coupling measurement of new particles. In addition, the reconstructed momenta from the constrained mass bound variables can be utilized to study the CP properties of the SM Higgs boson decaying to tau-lepton pairs. Similar studies can also be done for the semi-invisible decay of top pair production.

Bibliography

[1] S. L. Glashow. Partial Symmetries of Weak Interactions. *Nucl. Phys.*, 22:579–588, 1961.

[2] Steven Weinberg. A Model of Leptons. *Phys. Rev. Lett.*, 19:1264–1266, 1967.

[3] Georges Aad et al. Observation of a new particle in the search for the Standard Model Higgs boson with the ATLAS detector at the LHC. *Phys.Lett.*, B716:1–29, 2012, 1207.7214.

[4] Serguei Chatrchyan et al. Observation of a new boson at a mass of 125 GeV with the CMS experiment at the LHC. *Phys.Lett.*, B716:30–61, 2012, 1207.7235.

[5] David J. Gross and Frank Wilczek. Ultraviolet Behavior of Nonabelian Gauge Theories. *Phys. Rev. Lett.*, 30:1343–1346, 1973.

[6] H. David Politzer. Reliable Perturbative Results for Strong Interactions? *Phys. Rev. Lett.*, 30:1346–1349, 1973.

[7] Philip W. Anderson. Plasmons, Gauge Invariance, and Mass. *Phys. Rev.*, 130:439–442, 1963.

[8] Peter W. Higgs. Broken Symmetries and the Masses of Gauge Bosons. *Phys. Rev. Lett.*, 13:508–509, 1964.

[9] F. Englert and R. Brout. Broken Symmetry and the Mass of Gauge Vector Mesons. *Phys. Rev. Lett.*, 13:321–323, 1964.

[10] G. S. Guralnik, C. R. Hagen, and T. W. B. Kibble. Global Conservation Laws and Massless Particles. *Phys. Rev. Lett.*, 13:585–587, 1964.

[11] Arvindsai.S.Nair. Large hadron collider, August 2013. URL-http://www.slideshare.net/arvindsainair69/large-hadron-collider-25411885.

[12] G. Aad et al. The ATLAS Experiment at the CERN Large Hadron Collider. *JINST*, 3:S08003, 2008.

[13] S. Chatrchyan et al. The CMS experiment at the CERN LHC. *JINST*, 3:S08004, 2008.

[14] K. Aamodt et al. The ALICE experiment at the CERN LHC. *JINST*, 3:S08002, 2008.

[15] A. Augusto Alves, Jr. et al. The LHCb Detector at the LHC. *JINST*, 3:S08005, 2008.

[16] Tai Sakuma and Thomas McCauley. Detector and Event Visualization with SketchUp at the CMS Experiment. *J. Phys. Conf. Ser.*, 513:022032, 2014, 1311.4942.

[17] Four Peaks Technologies. Analyzing particles (cms), August 2013. URL-http://www.particlecentral.com/accelerator_page.html.

[18] Alan J. Barr and Christopher G. Lester. A Review of the Mass Measurement Techniques proposed for the Large Hadron Collider. *J.Phys.*, G37:123001, 2010, 1004.2732.

[19] A.J. Barr, T.J. Khoo, P. Konar, K. Kong, C.G. Lester, et al. Guide to transverse projections and mass-constraining variables. *Phys.Rev.*, D84:095031, 2011, 1105.2977.

[20] Kyoungchul Kong. Measuring Properties of Dark Matter at the LHC. *AIP Conf.Proc.*, 1604:381–388, 2014, 1309.6936.

[21] D.R. Tovey. Measuring the SUSY mass scale at the LHC. *Phys.Lett.*, B498:1–10, 2001, hep-ph/0006276.

[22] Jay Hubisz, Joseph Lykken, Maurizio Pierini, and Maria Spiropulu. Missing energy look-alikes with 100 pb^{-1} at the LHC. *Phys.Rev.*, D78:075008, 2008, 0805.2398.

[23] Partha Konar, Kyoungchul Kong, and Konstantin T. Matchev. $\sqrt{\hat{s}}_{min}$: A Global inclusive variable for determining the mass scale of new physics in events with missing energy at hadron colliders. *JHEP*, 0903:085, 2009, 0812.1042.

[24] Partha Konar, Kyoungchul Kong, Konstantin T. Matchev, and Myeonghun Park. RECO level $\sqrt{s}_{min}$ and subsystem $\sqrt{s}_{min}$: Improved global inclusive variables for measuring the new physics mass scale in $\not{E}_T$ events at hadron colliders. *JHEP*, 1106:041, 2011, 1006.0653.

[25] Won Sang Cho, Doojin Kim, Konstantin T. Matchev, and Myeonghun Park. Cracking the dark matter code at the LHC. *Phys.Rev.Lett.*, 112:211801, 2014, 1206.1546.

[26] Kaustubh Agashe, Doojin Kim, Manuel Toharia, and Devin G.E. Walker. Distinguishing Dark Matter Stabilization Symmetries Using Multiple Kinematic Edges and Cusps. *Phys.Rev.*, D82:015007, 2010, 1003.0899.

[27] Kaustubh Agashe, Doojin Kim, Devin G.E. Walker, and Lijun Zhu. Using M_{T2} to Distinguish Dark Matter Stabilization Symmetries. *Phys.Rev.*, D84:055020, 2011, 1012.4460.

[28] Gian Francesco Giudice, Ben Gripaios, and Rakhi Mahbubani. Counting dark matter particles in LHC events. *Phys.Rev.*, D85:075019, 2012, 1108.1800.

[29] Kaustubh Agashe, Roberto Franceschini, Doojin Kim, and Kyle Wardlow. Using Energy Peaks to Count Dark Matter Particles in Decays. *Phys. Dark Univ.*, 2:72–82, 2013, 1212.5230.

[30] Yang Bai and Hsin-Chia Cheng. Identifying Dark Matter Event Topologies at the LHC. *JHEP*, 1106:021, 2011, 1012.1863.

[31] Monika Blanke, David Curtin, and Maxim Perelstein. SUSY-Yukawa Sum Rule at the LHC. *Phys.Rev.*, D82:035020, 2010, 1004.5350.

[32] Arvind Rajaraman and Felix Yu. A New Method for Resolving Combinatorial Ambiguities at Hadron Colliders. *Phys.Lett.*, B700:126–132, 2011, 1009.2751.

[33] Philip Baringer, Kyoungchul Kong, Mathew McCaskey, and Daniel Noonan. Revisiting Combinatorial Ambiguities at Hadron Colliders with M_{T2}. *JHEP*, 1110:101, 2011, 1109.1563.

[34] Kiwoon Choi, Diego Guadagnoli, and Chan Beom Park. Reducing combinatorial uncertainties: A new technique based on MT2 variables. *JHEP*, 1111:117, 2011, 1109.2201.

[35] G.L. Bayatian et al. CMS technical design report, volume II: Physics performance. *J.Phys.*, G34:995–1579, 2007.

[36] I. Hinchliffe, F.E. Paige, M.D. Shapiro, J. Soderqvist, and W. Yao. Precision SUSY measurements at CERN LHC. *Phys.Rev.*, D55:5520–5540, 1997, hep-ph/9610544.

[37] B.K. Gjelsten, D.J. Miller, and P. Osland. Measurement of SUSY masses via cascade decays for SPS 1a. *JHEP*, 0412:003, 2004, hep-ph/0410303.

[38] B.C. Allanach, C.G. Lester, Michael Andrew Parker, and B.R. Webber. Measuring sparticle masses in nonuniversal string inspired models at the LHC. *JHEP*, 0009:004, 2000, hep-ph/0007009.

[39] Mihoko M. Nojiri, Daisuke Toya, and Tomio Kobayashi. Lepton energy asymmetry and precision SUSY study at hadron colliders. *Phys.Rev.*, D62:075009, 2000, hep-ph/0001267.

[40] B.K. Gjelsten, D.J. Miller, and P. Osland. Measurement of the gluino mass via cascade decays for SPS 1a. *JHEP*, 0506:015, 2005, hep-ph/0501033.

[41] Michael Burns, Konstantin T. Matchev, and Myeonghun Park. Using kinematic boundary lines for particle mass measurements and disambiguation in SUSY-like events with missing energy. *JHEP*, 0905:094, 2009, 0903.4371.

[42] Konstantin T. Matchev, Filip Moortgat, Luc Pape, and Myeonghun Park. Precise reconstruction of sparticle masses without ambiguities. *JHEP*, 0908:104, 2009, 0906.2417.

[43] M.M. Nojiri, G. Polesello, and D.R. Tovey. Proposal for a new reconstruction technique for SUSY processes at the LHC. 2003, hep-ph/0312317.

[44] K. Kawagoe, M.M. Nojiri, and G. Polesello. A New SUSY mass reconstruction method at the CERN LHC. *Phys.Rev.*, D71:035008, 2005, hep-ph/0410160.

[45] Hsin-Chia Cheng, John F. Gunion, Zhenyu Han, Guido Marandella, and Bob McElrath. Mass determination in SUSY-like events with missing energy. *JHEP*, 0712:076, 2007, 0707.0030.

[46] Mihoko M. Nojiri and Michihisa Takeuchi. Study of the top reconstruction in top-partner events at the LHC. *JHEP*, 0810:025, 2008, 0802.4142.

[47] Hsin-Chia Cheng, Dalit Engelhardt, John F. Gunion, Zhenyu Han, and Bob McElrath. Accurate Mass Determinations in Decay Chains with Missing Energy. *Phys.Rev.Lett.*, 100:252001, 2008, 0802.4290.

[48] Lars Sonnenschein. Analytical solution of ttbar dilepton equations. *Phys.Rev.*, D73:054015, 2006, hep-ph/0603011.

[49] C.G. Lester and D.J. Summers. Measuring masses of semiinvisibly decaying particles pair produced at hadron colliders. *Phys.Lett.*, B463:99–103, 1999, hep-ph/9906349.

[50] Alan Barr, Christopher Lester, and P. Stephens. m(T2): The Truth behind the glamour. *J.Phys.*, G29:2343–2363, 2003, hep-ph/0304226.

[51] Patrick Meade and Matthew Reece. Top partners at the LHC: Spin and mass measurement. *Phys.Rev.*, D74:015010, 2006, hep-ph/0601124.

[52] Christopher Lester and Alan Barr. MTGEN: Mass scale measurements in pair-production at colliders. *JHEP*, 0712:102, 2007, 0708.1028.

[53] Won Sang Cho, Kiwoon Choi, Yeong Gyun Kim, and Chan Beom Park. Gluino Stransverse Mass. *Phys.Rev.Lett.*, 100:171801, 2008, 0709.0288.

[54] Won Sang Cho, Kiwoon Choi, Yeong Gyun Kim, and Chan Beom Park. Measuring superparticle masses at hadron collider using the transverse mass kink. *JHEP*, 0802:035, 2008, 0711.4526.

[55] Alan J. Barr, Ben Gripaios, and Christopher G. Lester. Weighing Wimps with Kinks at Colliders: Invisible Particle Mass Measurements from End-points. *JHEP*, 0802:014, 2008, 0711.4008.

[56] Ben Gripaios. Transverse observables and mass determination at hadron colliders. *JHEP*, 0802:053, 2008, 0709.2740.

[57] Mihoko M. Nojiri, Yasuhiro Shimizu, Shogo Okada, and Kiyotomo Kawagoe. Inclusive transverse mass analysis for squark and gluino mass determination. *JHEP*, 0806:035, 2008, 0802.2412.

[58] Michael Burns, Kyoungchul Kong, Konstantin T. Matchev, and Myeonghun Park. Using Subsystem MT2 for Complete Mass Determinations in Decay Chains with Missing Energy at Hadron Colliders. *JHEP*, 0903:143, 2009, 0810.5576.

[59] Won Sang Cho, Jihn E. Kim, and Ji-Hun Kim. Amplification of endpoint structure for new particle mass measurement at the LHC. *Phys.Rev.*, D81:095010, 2010, 0912.2354.

[60] Won Sang Cho, William Klemm, and Mihoko M. Nojiri. Mass measurement in boosted decay systems at hadron colliders. *Phys.Rev.*, D84:035018, 2011, 1008.0391.

[61] Partha Konar, Kyoungchul Kong, Konstantin T. Matchev, and Myeonghun Park. Superpartner Mass Measurement Technique using 1D Orthogonal Decompositions of the Cambridge Transverse Mass Variable M_{T2}. *Phys.Rev.Lett.*, 105:051802, 2010, 0910.3679.

[62] Alan J. Barr, Ben Gripaios, and Christopher G. Lester. Transverse masses and kinematic constraints: from the boundary to the crease. *JHEP*, 0911:096, 2009, 0908.3779.

[63] Partha Konar, Kyoungchul Kong, Konstantin T. Matchev, and Myeonghun Park. Dark Matter Particle Spectroscopy at the LHC: Generalizing M(T2) to Asymmetric Event Topologies. *JHEP*, 1004:086, 2010, 0911.4126.

[64] Colin H. Lally and Christopher G. Lester. Properties of MT2 in the massless limit. 2012, 1211.1542.

[65] Daniel R. Tovey. On measuring the masses of pair-produced semi-invisibly decaying particles at hadron colliders. *JHEP*, 0804:034, 2008, 0802.2879.

[66] Giacomo Polesello and Daniel R. Tovey. Supersymmetric particle mass measurement with the boost-corrected contransverse mass. *JHEP*, 1003:030, 2010, 0910.0174.

[67] Mario Serna. A Short comparison between m(T2) and m(CT). *JHEP*, 0806:004, 2008, 0804.3344.

[68] Konstantin T. Matchev and Myeonghun Park. A General method for determining the masses of semi-invisibly decaying particles at hadron colliders. *Phys.Rev.Lett.*, 107:061801, 2011, 0910.1584.

[69] Rakhi Mahbubani, Konstantin T. Matchev, and Myeonghun Park. Reinterpreting the Oxbridge stransverse mass variable MT2 in general cases. *JHEP*, 1303:134, 2013, 1212.1720.

[70] Won Sang Cho, James S. Gainer, Doojin Kim, Konstantin T. Matchev, Filip Moortgat, et al. On-shell constrained M_2 variables with applications to mass measurements and topology disambiguation. *JHEP*, 1408:070, 2014, 1401.1449.

[71] Abdelhak Djouadi. The Anatomy of electro-weak symmetry breaking. II. The Higgs bosons in the minimal supersymmetric model. *Phys.Rept.*, 459:1–241, 2008, hep-ph/0503173.

[72] Matthew Baumgart, Thomas Hartman, Can Kilic, and Lian-Tao Wang. Discovery and measurement of sleptons, binos, and winos with a Z-prime. *JHEP*, 0711:084, 2007, hep-ph/0608172.

[73] Mirjam Cvetic and P. Langacker. Z-prime physics and supersymmetry. *Adv.Ser.Direct.High Energy Phys.*, 21:325–350, 2010, hep-ph/9707451.

[74] Hsin-Chia Cheng, Jonathan L. Feng, and Konstantin T. Matchev. Kaluza-Klein dark matter. *Phys.Rev.Lett.*, 89:211301, 2002, hep-ph/0207125.

[75] AseshKrishna Datta, Kyoungchul Kong, and Konstantin T. Matchev. Discrimination of supersymmetry and universal extra dimensions at hadron colliders. *Phys.Rev.*, D72:096006, 2005, hep-ph/0509246.

[76] Gulab Bambhaniya, Joydeep Chakrabortty, Srubabati Goswami, and Partha Konar. Generation of neutrino mass from new physics at TeV scale and multilepton signatures at the LHC. *Phys.Rev.*, D88(7):075006, 2013, 1305.2795.

[77] Neil D. Christensen, Tao Han, Zhuoni Qian, Josh Sayre, Jeonghyeon Song, et al. Determining the Dark Matter Particle Mass through Antler Topology Processes at Lepton Colliders. *Phys.Rev.*, D90:114029, 2014, 1404.6258.

[78] Andreas Papaefstathiou and Bryan Webber. Effects of QCD radiation on inclusive variables for determining the scale of new physics at hadron colliders. *JHEP*, 0906:069, 2009, 0903.2013.

[79] Andreas Papaefstathiou and Bryan Webber. Effects of invisible particle emission on global inclusive variables at hadron colliders. *JHEP*, 1007:018, 2010, 1004.4762.

[80] A. Barr, T. Khoo, P. Konar, K. Kong, C. Lester, et al. A Storm in a 'T' Cup. *AIP Conf.Proc.*, 1441:722–724, 2012, 1108.5182.

[81] Won Sang Cho, Kiwoon Choi, Yeong Gyun Kim, and Chan Beom Park. M(T2)-assisted on-shell reconstruction of missing momenta and its application to spin measurement at the LHC. *Phys.Rev.*, D79:031701, 2009, 0810.4853.

[82] Chan Beom Park. Reconstructing the heavy resonance at hadron colliders. *Phys.Rev.*, D84:096001, 2011, 1106.6087.

[83] Chrisopher G. Lester and Benjamin Nachman. Bisection-based asymmetric M_{T2} computation: a higher precision calculator than existing symmetric methods. *JHEP*, 03:100, 2015, 1411.4312.

[84] Tao Han, Ian-Woo Kim, and Jeonghyeon Song. Kinematic Cusps: Determining the Missing Particle Mass at Colliders. *Phys.Lett.*, B693:575–579, 2010, 0906.5009.

[85] Tao Han, Ian-Woo Kim, and Jeonghyeon Song. Kinematic Cusps With Two Missing Particles I: Antler Decay Topology. *Phys.Rev.*, D87(3):035003, 2013, 1206.5633.

[86] Diego Guadagnoli and Chan Beom Park. M_{T2}-reconstructed invisible momenta as spin analizers, and an application to top polarization. *JHEP*, 1401:030, 2014, 1308.2226.

[87] Abhaya Kumar Swain and Partha Konar. Constrained $\sqrt{\hat{S}_{min}}$ and reconstructing with semi-invisible production at hadron colliders. *JHEP*, 1503:142, 2015, 1412.6624.

[88] Abhaya Kumar Swain and Partha Konar. Mass determination and event reconstruction at Large Hadron Collider. *Springer Proc. Phys.*, 174:599–603, 2016, 1507.01792.

[89] The CMS Collaborations. Cms higgs physics publications, December 2015. URL-http://cms-results.web.cern.ch/cms-results/public-results/publications/HIG/TAUTAU.html.

[90] The ATLAS Collaborations. Atlas higgs physics public results, December 2015. URL-https://twiki.cern.ch/twiki/bin/view/AtlasPublic/HiggsPublicResults.

[91] Serguei Chatrchyan et al. Evidence for the 125 GeV Higgs boson decaying to a pair of τ leptons. *JHEP*, 05:104, 2014, 1401.5041.

[92] Higgs decay to $\tau^+\tau^-$ a possible signature of intermediate mass higgs bosons at high energy hadron colliders. *Nuclear Physics B*, 297(2):221 – 243, 1988.

[93] A. Elagin, P. Murat, A. Pranko, and A. Safonov. A New Mass Reconstruction Technique for Resonances Decaying to di-tau. *Nucl. Instrum. Meth.*, A654:481–489, 2011, 1012.4686.

[94] Li-Gang Xia. An improved mass reconstruction technique for a heavy resonance decaying to $\tau^+\tau^-$. 2016, 1601.02454.

[95] Ben Gripaios, Keiko Nagao, Mihoko Nojiri, Kazuki Sakurai, and Bryan Webber. Reconstruction of Higgs bosons in the di-tau channel via 3-prong decay. *JHEP*, 03:106, 2013, 1210.1938.

[96] Sho Maruyama. Stochastic mass-reconstruction: a new technique to reconstruct resonance masses of heavy particles decaying into tau lepton pairs. 2015, 1512.04842.

[97] Torbjorn Sjostrand, Stephen Mrenna, and Peter Z. Skands. A Brief Introduction to PYTHIA 8.1. *Comput. Phys. Commun.*, 178:852–867, 2008, 0710.3820.

[98] Jeffrey D. Anderson, Matthew H. Austern, and Robert N. Cahn. Measurement of Z-prime couplings at future hadron colliders through decays to tau leptons. *Phys. Rev.*, D46:290–302, 1992.

[99] Partha Konar and Abhaya Kumar Swain. Mass reconstruction with M_2 under constraint in semi-invisible production at a hadron collider. *Phys. Rev.*, D93:015021, 2016, 1509.00298.

[100] Roni Harnik, Adam Martin, Takemichi Okui, Reinard Primulando, and Felix Yu. Measuring CP violation in $h \to \tau^+\tau^-$ at colliders. *Phys. Rev.*, D88(7):076009, 2013, 1308.1094.

[101] S. Berge, W. Bernreuther, B. Niepelt, and H. Spiesberger. How to pin down the CP quantum numbers of a Higgs boson in its tau decays at the LHC. *Phys. Rev.*, D84:116003, 2011, 1108.0670.